Draft version September 28, 2022
Typeset using LaTeX **preprint2** style in AASTeX631

Rotating Solar Models in Agreement with Helioseismic Results and Updated Neutrino Fluxes

Wuming Yang[1]

[1] *Department of Astronomy, Beijing Normal University, Beijing 100875, China*

ABSTRACT

Standard solar models (SSMs) constructed in accordance with old solar abundances are in reasonable agreement with seismically inferred results, but SSMs with new low-metal abundances disagree with the seismically inferred results. The constraints of neutrino fluxes on solar models exist in parallel with those of helioseismic results. The solar neutrino fluxes were updated by Borexino Collaboration. We constructed rotating solar models with new low-metal abundances where the effects of enhanced diffusion and convection overshoot were included. A rotating model using OPAL opacities and the Caffau abundance scale has better sound-speed and density profiles than the SSM with the old solar abundances and reproduces the observed p-mode frequency ratios r_{02} and r_{13}. The depth and helium abundance of the convection zone of the model agree with the seismically inferred ones at the level of 1σ. The updated neutrino fluxes are also reproduced by the model at the level of 1σ. The effects of rotation and enhanced diffusion not only improve the model's sound-speed and density profiles but bring the neutrino fluxes predicted by the model into agreement with the detected ones. Moreover, the calculations show that OP may underestimate opacities for the regions of the Sun with $T \gtrsim 5 \times 10^6$ K by around 1.5%, while OPAL may underestimate opacities for the regions of the Sun with 2×10^6 K $\lesssim T \lesssim 5 \times 10^6$ K by about $1 - 2\%$.

Keywords: Solar abundances — Helioseismology — Solar interior — Solar neutrino fluxes — Solar rotation

1. INTRODUCTION

The heavy-element abundance Z_s of the Sun, derived by Grevesse & Sauval (1998, hereafter GS98) from photospheric spectroscopy, is 0.017, whose uncertainty is of the order of 10 percent. The ratio of the heavy-element abundance to hydrogen abundance is 0.0231. Since Lodders (2003) and Asplund et al. (2005) reassessed the value of the Z_s, it has been revised several times (Lodders et al. 2009; Asplund et al. 2009; Caffau et al. 2010, 2011; Lodders 2020; Asplund et al. 2021; Amarsi et al. 2021). The well-known values of the new Z_s are 0.0133 (Lodders 2003), 0.0122 (Asplund et al. 2005), 0.0141 (Lodders et al. 2009), or 0.0134 (Asplund et al. 2009, hereafter AGSS09). These revised values are obviously lower than the old one.

The helium abundance, Y_s, in the solar convection zone (CZ) and thus photosphere can-

yangwuming@bnu.edu.cn

not be inferred directly from spectroscopy, but can be determined by helioseismology. The values of seismically inferred Y_s and Z_s are 0.2485 ± 0.0035 (Basu & Antia 2004; Serenelli & Basu 2010) and 0.0172 ± 0.002 (Antia & Basu 2006), respectively. However, the values given by Vorontsov et al. (2013) or Vorontsov et al. (2014) are in the range of $Y_s = 0.240$–0.255 and $Z_s = 0.008$–0.013 or $Y_s = 0.245$–0.260 and $Z_s = 0.006$–0.011. Moreover, the value of Z_s inferred by Buldgen et al. (2017) is in the range of 0.008–0.014. The radius of the base of the CZ (BCZ) also can be determined by helioseismology. The inferred radius of the BCZ is $0.713 \pm 0.003\ R_\odot$ (Christensen-Dalsgaard et al. 1991) or $0.713 \pm 0.001\ R_\odot$ (Basu & Antia 1997).

The standard solar models (SSMs) constructed in accordance with the high metal abundances (old solar abundances, e.g. GS98) are considered to be in good agreement with the seismically inferred sound-speed and density profiles, depth and helium abundance of the CZ, but the SSMs constructed in accordance with the low metal abundances (revised solar abundances) do not completely agree with the seismically inferred results (Bahcall et al. 2004; Basu & Antia 2004; Yang & Bi 2007; Basu et al. 2009; Serenelli et al. 2009, 2011; Zhang & Li 2012) and the neutrino flux constraints (Bahcall & Pinsonneault 2004; Turck-Chièze et al. 2010, 2011; Turck-Chièze & Couvidat 2011; Yang 2016), which is known as solar modeling problem or solar abundance problem (Basu et al. 2015; Christensen-Dalsgaard 2021; Salmon et al. 2021; Amarsi et al. 2021).

In order to reconcile the low-Z models with helioseismology, many physical effects have been studied. For example, increased opacity at the base of the CZ was studied by Bahcall et al. (2004), Serenelli et al. (2009), and Buldgen et al. (2019); enhanced neon abundance was suggested by Bahcall et al. (2005); mass accretion of metal-rich/poor material or helium-poor material was investigated by Castro et al. (2007), Guzik & Mussack (2010), Serenelli et al. (2011), and Zhang et al. (2019); overshooting below the CZ was used to recover the CZ depth (Montalbán et al. 2006; Castro et al. 2007; Yang 2019; Zhang et al. 2019).

In order to match the seismically inferred sound-speed and density profiles (Basu et al. 2000, 2009), the gravitational settling that reduces the surface helium abundance by about 11% ($\sim$ 0.03 by mass fraction) below its initial value is required in SSMs. Macroscopic turbulent mixing can reduce the amount of surface helium settling by around 40% (Proffitt & Michaud 1991). The effects of the turbulent mixing on the diffusion and settling of helium and heavy elements were not considered in the diffusion coefficients of Thoul et al. (1994). Asplund et al. (2004) suggested that enhanced diffusion and settling of helium and heavy elements might be able to reconcile the low-Z models with helioseismology. The increased diffusion can significantly improve sound-speed and density profiles, but leaves the CZ helium abundance too low (Basu & Antia 2004; Montalbán et al. 2004; Guzik et al. 2005; Yang 2019).

Rotational mixing can transport helium outward. It thus can counteract the effect of enhanced diffusion on the surface helium abundance (Yang 2019), i.e., it can improve the prediction of the surface helium abundance. The effects of rotation on the low-Z models were studied by Yang & Bi (2007), Turck-Chièze et al. (2010, 2011), and Yang (2016, 2019). However, the rotating models with AGSS09 mixtures (Yang 2019) disagree with the detected neutrino fluxes of Borexino Collaboration (2018, 2020).

Bahcall & Pinsonneault (2004) and Serenelli et al. (2009) found that an $11\% - 20\%$ increase in OPAL opacities at the BCZ can reconcile the low-Z models with helioseismology. Badnell et al. (2005) showed that in the region OP opacity is slightly larger than OPAL opacity but no more than 2.5 percent. Buldgen et al. (2019) concluded that the solar modeling problem likely occurs from multiple small contributors. Opacity could be one of the contributors.

The production of solar neutrinos is sensitive to the central properties of the Sun. The ^{8}B neutrino flux is strongly dependent on the central temperature of the Sun (Bahcall & Ulrich 1988; Turck-Chièze & Couvidat 2011). The determinations of solar neutrino fluxes complement helioseismology in diagnosing the core of the Sun. The constraints of neutrino fluxes on solar models exist in parallel with those of helioseismology and are studied by many authors (Bahcall & Pinsonneault 2004; Turck-Chièze et al. 2010, 2011; Turck-Chièze & Couvidat 2011; Yang 2016, 2019; Zhang et al. 2019). Borexino Collaboration (2018, 2020) updated solar neutrino fluxes and determined the total fluxes of ^{13}N, ^{15}O, and ^{17}F neutrinos. Their ^{8}B neutrino flux is higher than that determined by Bergström et al. (2016). The low-Z model of Zhang et al. (2019) with helium-poor accretion and solar-wind mass loss agrees with helioseismic results but disagrees with the neutrino fluxes detected by Borexino Collaboration (2018, 2020). Moreover, Salmon et al. (2021) showed that the updated solar neutrino fluxes prefer high-metallicity solar models. The solar modeling problem has persisted for almost 20 years.

Caffau et al. (2010, 2011) independently analysed carbon, nitrogen, and oxygen abundances in the solar photosphere. They found that the heavy-element abundance of the solar surface is $Z_s = 0.0154/0.0153$, supplemented with data from Lodders et al. (2009). The value of Z_s/X_s advocated by Caffau et al. (2011) is 0.0209. These values are larger than those of Lodders et al. (2009) and AGSS09. Hope et al. (2020) studied the possible origin of the solar abundance problem. Their result favors the solar Z_s reported by Caffau et al. (2011) rather than the measurement by AGSS09.

Lodders (2020) reanalysed the solar photospheric abundances and recommended $Z_s = 0.0149$ and $Z_s/X_s = 0.0201$. Asplund et al. (2021, hereafter AAG21) also reassessed the solar abundances with updated atomic data and a 3D radiative-hydrodynamical model of the solar photosphere. They advocated $Z_s = 0.0139 \pm 0.0006$, $Y_s = 0.2423 \pm 0.0054$, and $Z_s/X_s = 0.0187 \pm 0.0009$. Moreover, using the 3D radiative-hydrodynamical model of solar photosphere, Amarsi et al. (2021) analysed 408 molecular lines of C, N, and O and obtained solar C, N, and O abundances, which are slightly larger than their previous results in AAG21. With these molecular abundances, the value of the heavy-element abundance of the solar surface increases from $Z_s = 0.0139$ to $Z_s = 0.0142$ (Amarsi et al. 2021). This increase indicates that "it may be worthwhile to continue improving the atomic and molecular data as well as the model atmospheres and line formation methods" (Amarsi et al. 2021).

In this work, we mainly focus on whether the solar models constructed in accordance with AAG21 mixtures and Caffau et al. (2011) mixtures agree with the seismically inferred results and updated neutrino fluxes. The paper is organized as follows. Input physics in models are introduced in Section 2, calculation results are presented in Section 3, and discussion and summary are given in Section 4.

2. INPUT PHYSICS IN MODELS

All solar models were calculated by using the Yale Rotating Stellar Evolution Code (Pinsonneault et al. 1989; Yang & Bi 2007; Demarque et al. 2008) in its rotation and non-rotation configurations. The frequencies of p-modes of models were computed by using the Guenther (1994) pulsation code. The OPAL equation-of-state (EOS2005) tables (Rogers & Nayfonov 2002), OPAL (Iglesias & Rogers 1996) and OP opacity tables (Seaton 1987; The Opacity Project Team 1995; Badnell et al. 2005; Delahaye et al. 2016) were used, supplemented by the Ferguson et al. (2005) opacity tables at low temperature. The opacity tables were reconstructed with the GS98, Caffau et al. (2011), and AAG21 mixtures (see Appendix A). The nuclear reaction rates were calculated with the subroutine of Bahcall & Pinsonneault (1992) and Bahcall et al. (1995, 2001) (see Appendix B). Convection was determined by the Schwarzschild criterion and treated according to the standard mixing-length theory (Böhm-Vitense 1958; Kippenhahn et al. 2012). The overshoot region below the BCZ was assumed to be both fully mixed and adiabatically stratified (Christensen-Dalsgaard et al. 1991). The depth of the overshoot region is determined by $\delta_{\rm ov} H_p$ (Demarque et al. 2008), where $\delta_{\rm ov}$ is a free parameter and H_p is the local pressure scale height. A convection overshoot of $\delta_{\rm ov} \approx 0.1$ is required to recover the seismically inferred depth of the CZ in our rotating models. The diffusion and settling of both helium and heavy elements were computed using the formulas of Thoul et al. (1994). In the atmosphere, Krishna Swamy (1966) $T-\tau$ relation was adopted.

We treated the transport of angular momentum and material mixing as a diffusion process (Endal & Sofia 1978), i.e.

$$\frac{\partial \Omega}{\partial t} = f_{\Omega} \frac{1}{\rho r^4} \frac{\partial}{\partial r}(\rho r^4 D \frac{\partial \Omega}{\partial r}) \tag{1}$$

for the transport of angular momentum and

$$\begin{aligned} \frac{\partial X_i}{\partial t} = & f_c f_{\Omega} \frac{1}{\rho r^2} \frac{\partial}{\partial r}(\rho r^2 D \frac{\partial X_i}{\partial r}) \\ & +(\frac{\partial X_i}{\partial t})_{\rm nuc} - \frac{1}{\rho r^2} \frac{\partial}{\partial r}(f_0 \rho r^2 X_i V_i) \end{aligned} \tag{2}$$

for the change in the mass fraction X_i of chemical species i, where D is the diffusion coefficient caused by rotational instabilities including the Eddington circulation, the Goldreich-Schubert-Fricke instability (Pinsonneault et al. 1989), and the secular shear instability of Zahn (1993). The default values of f_{Ω} and f_c are 1 and 0.03 (Yang 2019), respectively. We applied a straight multiplier f_0 to the diffusion velocity V_i to enhance the rates of diffusion and settling, as Basu & Antia (2004), Montalbán et al. (2004), Guzik et al. (2005), and Yang (2019) have done, despite the fact that there is no obvious physical justification for such a multiplier. The value of f_0 is 1 for standard cases but larger than 1 for an enhanced diffusion model. The angular-momentum loss from the CZ due to magnetic braking was calculated with Kawaler's relation (Kawaler 1988; Chaboyer et al 1995). More details of calculation for rotation were described in Pinsonneault et al. (1989) and Yang (2019).

All models were evolved from a homogeneous zero-age main-sequence model to the present solar age 4.57 Gyr, luminosity 3.844×10^{33} erg s^{-1}, radius 6.9598×10^{10} cm, and mass 1.9891×10^{33} g (Bahcall et al. 1995). The initial metallicity Z_0, hydrogen abundance X_0, and mixing-length parameter $\alpha_{\rm MLT}$ are free parameters. They were adjusted to match the constraints of luminosity and radius within around 10^{-5} and observed Z_s/X_s. The initial helium abundance is determined by $Y_0 = 1 - X_0 - Z_0$. The value of $\alpha_{\rm MLT}$ changes with input physics, i.e. a new solar calibration of $\alpha_{\rm MLT}$ is performed each time the input physics change. The initial rotation rate, Ω_i of rotating models was adjusted to reproduce the solar equatorial velocity of about 2.0 km s^{-1}. The values of these parameters are shown in Table 1.

3. CALCULATION RESULTS

3.1. *Solar Models with High Metal Abundances*

3.1.1. *The Models Constructed with OPAL Opacity Tables*

Using the OPAL opacity tables constructed with GS98 mixtures, we computed SSM GS98M and rotating model GS98Mr. The central temperature and density, surface helium and heavy-element abundances, radius of the BCZ, and other parameters of the models are listed in Table 1. The fluxes of *pp*, *pep*, *hep*, ^{7}Be, ^{8}B, ^{13}N, ^{15}O, and ^{17}F neutrinos calculated from the models are given in Table 2. Table 3 lists some of the physical configurations of each model.

The surface heavy-element abundance of 0.0174 of GS98M is in agreement with that determined by GS98. The surface helium abundance and r_{cz} of GS98M are also consistent with the seismically inferred ones (see Table 1). We compared the sound speed and density of models with those inferred by Basu et al. (2009) using the data from the Birmingham Solar-Oscillations Network (Chaplin et al. 1996) and the Michelson Doppler Imager (Schou et al. 1998). The values of relative sound-speed difference, $\delta c_s/c_s$, and density difference, $\delta\rho/\rho$, between the Sun and GS98M are less than 0.0043 and 0.028, respectively (see Figure 1). Moreover, the ratios of small to large frequency separations, r_{02} and r_{13} (Roxburgh & Vorontsov 2003), of the model agree with those calculated from observed frequencies of Chaplin et al. (1999) or García et al. (2011) (see Figure 2). Table 4 gives the values of $\chi^2_{c_s+\rho}$ and $\chi^2_{d_{02+13}}$ of the models.

We compared the neutrino fluxes computed from models with those determined by different authors (Bellini et al. 2011, 2012; Ahmed et al. 2004; Bergström et al. 2016; Borexino Collaboration 2018, 2020) and ones predicted by the models BP04 (Bahcall & Pinsonneault 2004) and SSeM (Turck-Chièze & Couvidat 2011) in Table 2. The neutrino fluxes of GS98M are comparable with those of BP04. Some differences between the nuclear cross-section factors S_0 (Bahcall 1989) used in BP04 and those used in GS98M are listed in Table 6 of Appendix B. The total fluxes of ^{13}N, ^{15}O, and ^{17}F neutrinos calculated from GS98M are $\Phi(\mathrm{CNO}) = 10.2\times10^8$ cm^{-2} s^{-1}, slightly larger than $7^{+3}_{-2}\times10^8$ cm^{-2} s^{-1} detected by Borexino Collaboration (2020). The *pp*, *pep*, *hep*, ^{7}Be, and ^{8}B neutrino fluxes of GS98M are in agreement with those determined by Borexino Collaboration (2018). However, the fluxes of ^{7}Be and ^{8}B neutrinos are larger than those determined by Bergström et al. (2016) (see Table 2).

Figure 1 shows that the effects of rotation can significantly improve the sound-speed and density profiles. The value of the relative sound-speed difference, $\delta c_s/c_s$, below the CZ can be decreased by about 50%. Moreover, the centrifugal effect leads to a decrease in the central temperature. The fluxes of ^{7}Be, ^{8}B, ^{13}N, ^{15}O, and ^{17}F neutrinos are sensitive to the central temperature. Thus the fluxes calculated from rotating models are generally lower than those computed from non-rotating models (see Table 2). The total fluxes of ^{13}N, ^{15}O, and ^{17}F neutrinos of GS98Mr are $\Phi(\mathrm{CNO}) = 9.5\times10^8$ cm^{-2} s^{-1}, which are in agreement with the detected value of $7^{+3}_{-2}\times10^8$ cm^{-2} s^{-1}. The ^{8}B neutrino flux of 5.29×10^6 cm^{-2} s^{-1} for GS98Mr is consistent with $5.16^{+0.13}_{-0.09}\times10^6$ cm^{-2} s^{-1} determined by Bergström et al. (2016) and $5.68^{+0.39}_{-0.41}\times10^6$ cm^{-2} s^{-1} detected by Borexino Collaboration (2018). However, the surface helium abundance of 0.2534 of GS98Mr is higher than the inferred value of 0.2485 ± 0.0035. Thus the high-Z models constructed with OPAL opacities do not completely agree with helioseismic results and updated neutrino fluxes.

3.1.2. *The Models Constructed with OP Opacity Tables*

In order to study the effects of opacities, we constructed SSM GS98op and rotating model GS98opr by using OP opacity tables. Tables 1 and 2 list the fundamental parameters and neutrino fluxes of the models, respectively. For almost the same metallicity, OP opacities are larger by about $0-2\%$ than OPAL opacities in the region of the Sun with $0.5\ R_\odot \lesssim r \lesssim 0.8\ R_\odot$ but smaller by about $1-2\%$ in the region with $r \lesssim 0.4\ R_\odot$ (see Figure 3). The sound-speed and density profiles and frequency sepa-

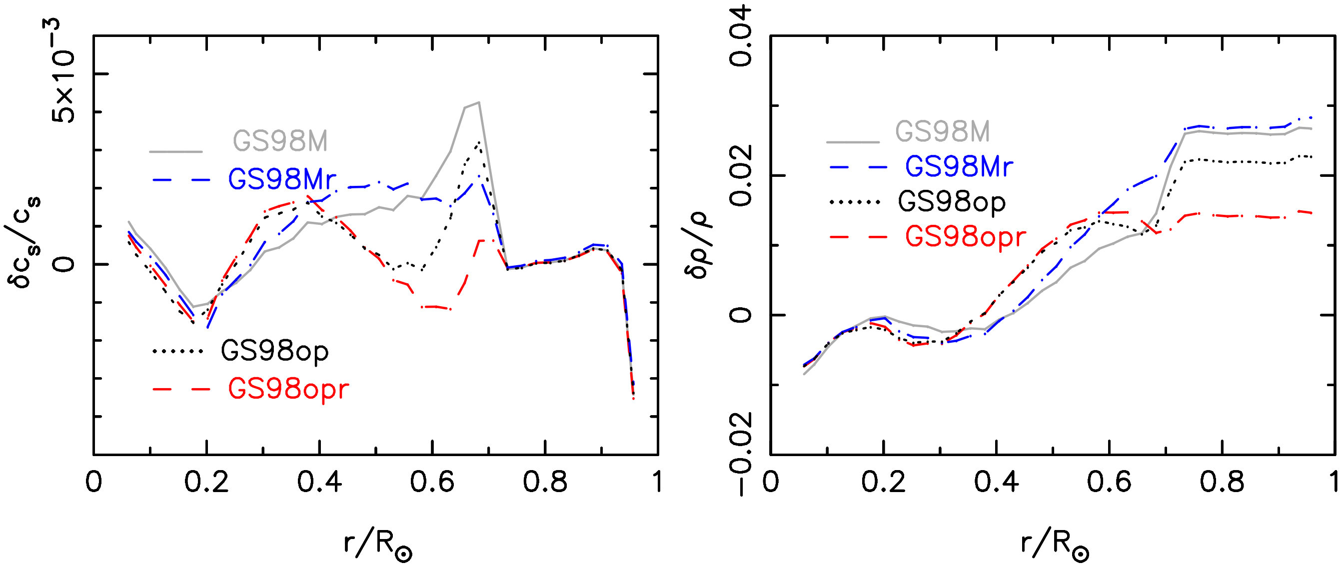

Figure 1. Relative sound-speed and density differences, in the sense (Sun-Model)/Model, between the Sun and models. The solar sound speed and density are given in Basu et al. (2009).

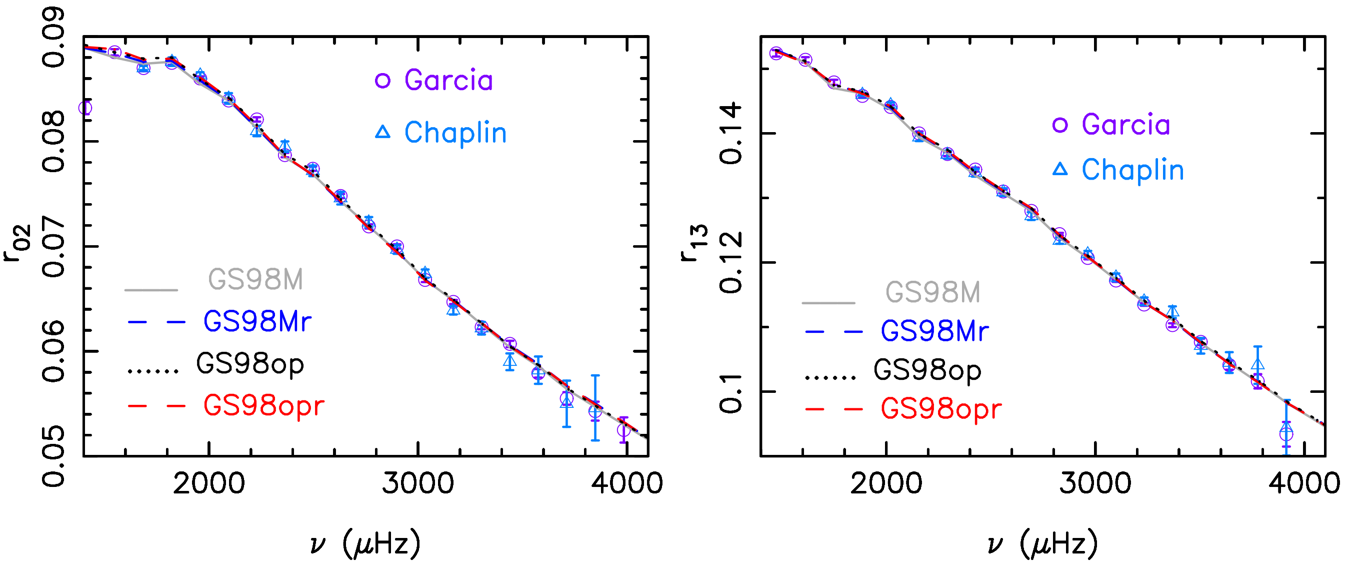

Figure 2. Distributions of observed and predicted ratios r_{02} and r_{13} as a function of frequency. The circles and triangles show the ratios calculated from the frequencies observed by GOLF & VIRGO (García et al. 2011) and BiSON (Chaplin et al. 1999), respectively.

ration ratios of the models are shown in Figures 1 and 2, respectively, which show that OP has almost no improvement in the reproduction of the frequency separation ratios in comparison to OPAL (see Figure 2), but obviously improves density profile and the sound-speed profile below the CZ where OP opacities are mainly larger than OPAL opacities. OP slightly worsens the sound-speed profile in the inner layers of radiative region where OP opacities are lower than OPAL opacities (see Figures 1 and 3).

In order to obtain the same surface heavy-element abundance and the solar luminosity and radius at the age of 4.57 Gyr, the decrease in opacities requires decreasing the initial helium abundance and changing α_{MLT}. As a consequence, the surface helium abundances of the models constructed with OP opacity tables are

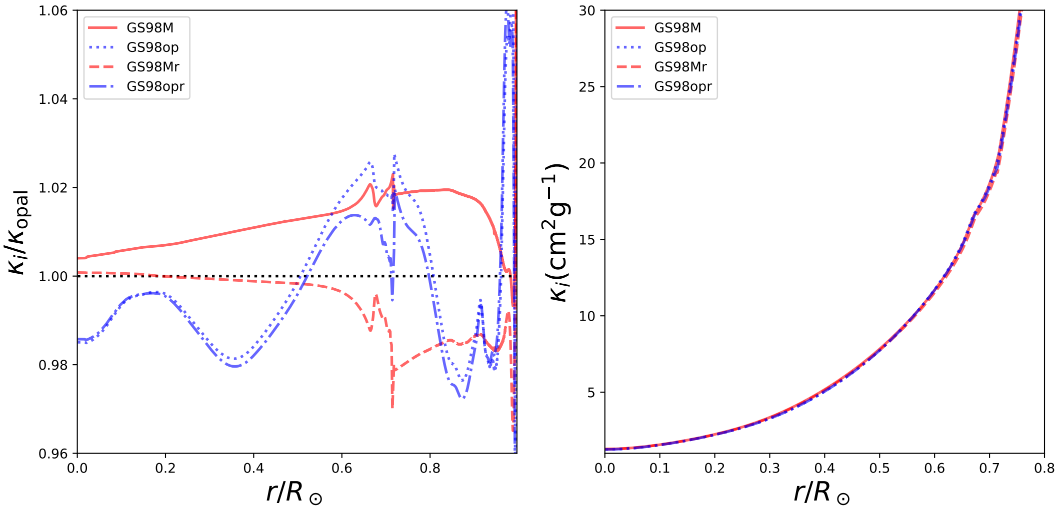

Figure 3. Left panel: comparison of Rosseland mean opacity of different models relative to that of a reference model constructed with OPAL opacity tables and $Z_s = 0.0170$. Right panel: distributions of Rosseland mean opacity of the models as a function of radius.

lower than those of the models constructed with OPAL opacity tables. The surface helium abundance of 0.2414 for GS98op is smaller than the inferred value of 0.2485 ± 0.0035. Therefore, GS98op is not a good SSM.

Rotational mixing brings hydrogen into inner layers from outer layers and transports helium outward, i.e. decreases the hydrogen abundance in the CZ, but increases the hydrogen abundance in the region with $0.5\ R_\odot \lesssim r \lesssim 0.7\ R_\odot$ (see Figure 4), which changes the distribution of the mean molecular weight. As a consequence, the density and sound-speed profiles are significantly improved by the effects of rotation. The value of the relative sound-speed difference below the CZ is decreased by about 80% (see Figure 1). Although OP improves the sound-speed profile below the CZ, the effects of rotation play a more important role in improving the sound-speed profile. Moreover, the amount of the CZ helium settling is reduced by about 34%. The surface helium abundance of 0.2511 for GS98opr is in agreement with the seismically inferred value of 0.2485 ± 0.0035, and increased by about 0.01 compared to that of the non-rotating model.

The central temperatures of models constructed with OP opacity tables are lower than those of models constructed with OPAL opacity tables. Therefore, the fluxes of ^{7}Be, ^{8}B, ^{13}N, ^{15}O, and ^{17}F neutrinos computed from GS98op and GS98opr are smaller than those calculated from GS98M and GS98Mr. The total fluxes Φ(CNO) of GS98op and GS98opr are in agreement with that detected by Borexino Collaboration (2020). The ^{8}B neutrino fluxes of the models are consistent with that determined by Bergström et al. (2016) but lower than one detected by Borexino Collaboration (2018). Thus the high-Z models constructed with OP opacities also do not completely agree with helioseismic results and updated neutrino fluxes.

We chose GS98M as the best SSM and GS98opr as the best rotating model with high metal abundances and went on to construct the models with low metal abundances and compare them with these two models.

3.2. *Solar Models with Low Metal Abundances*

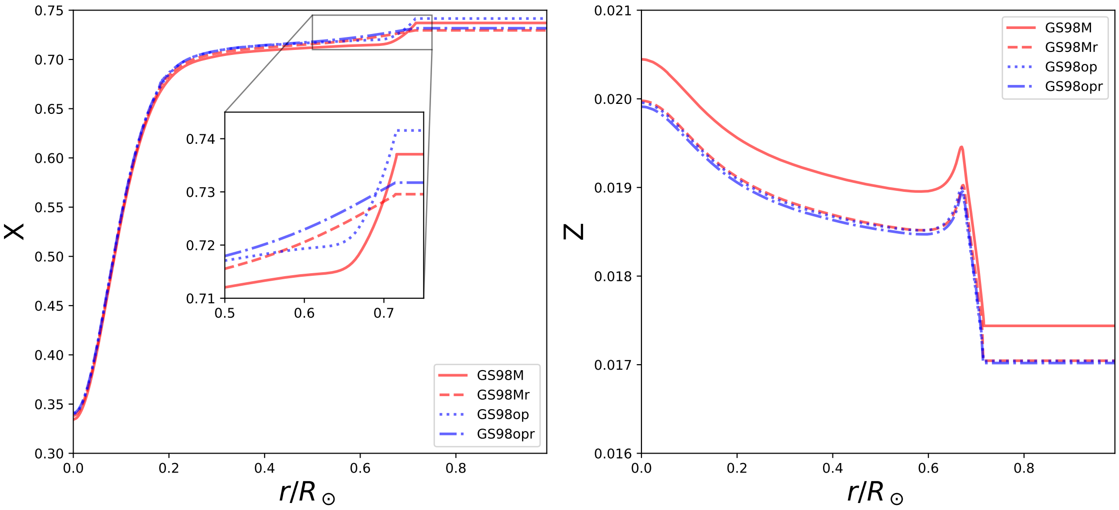

Figure 4. Distributions of hydrogen and metal abundances of models as a function of radius.

3.2.1. *Standard and Rotating Models*

Using OP opacity tables reconstructed with AAG21 mixtures, we computed SSM Aop01 and rotating model Aop01r with the surface heavy-element abundance determined by Asplund et al. (2021). Although OP opacities and the effects of rotation can significantly improve sound-speed and density profiles, the sound-speed and density profiles of Aop01 and Aop01r are not as good as those of GS98M (see Figure 5). The models also can not reproduce the observed frequency separation ratios r_{02} and r_{13} (see Figure 6 or Table 4) and inferred helium abundance. The total fluxes Φ(CNO) of Aop01 and Aop01r are in agreement with the detection of Borexino Collaboration (2020), but their ^{7}Be and ^{8}B neutrino fluxes are too low (see Table 2).

With the heavy-element abundance determined by Lodders (2020), we constructed SSM Aop02 and rotating model Aop02r. We also calculated SSM Cop01 and rotating model Cop01r by using the OP opacity tables reconstructed with Caffau et al. (2011) mixtures. The SSMs Aop02 and Cop01 obviously disagree with seismically inferred results and detected ^{8}B neutrino flux. For rotating models Aop02r and Cop01r, the overshoot of convection brings the depth of the CZ into agreement with the seismically inferred one. The surface helium abundances of Aop02r and Cop01r are 0.2453 and 0.2467, respectively, consistent with the inferred value of 0.2485 ± 0.0035. The total fluxes Φ(CNO) predicted by Aop02r and Cop01r are 7.4 and 7.6×10^8 cm^{-2} s^{-1}, respectively, which are in good agreement with that detected by Borexino Collaboration (2020). The sound-speed profiles of Aop02r and Cop01r are comparable with that of GS98M (see Figure 5). The observed frequency separation ratios r_{02} and r_{13} are almost reproduced by the models (see Figure 6). However, the ^{8}B neutrino fluxes of Aop02r and Cop01r are obviously lower than those determined by Bergström et al. (2016) and Borexino Collaboration (2018) (see Table 2). Moreover, their density profiles are not as good as that of GS98M. These indicate that the effects of OP and rotation can improve the solar model but can not completely solve the solar modeling problem.

3.2.2. *Rotating and Enhanced Diffusion Models Constructed in Accordance with AAG21 Mixtures*

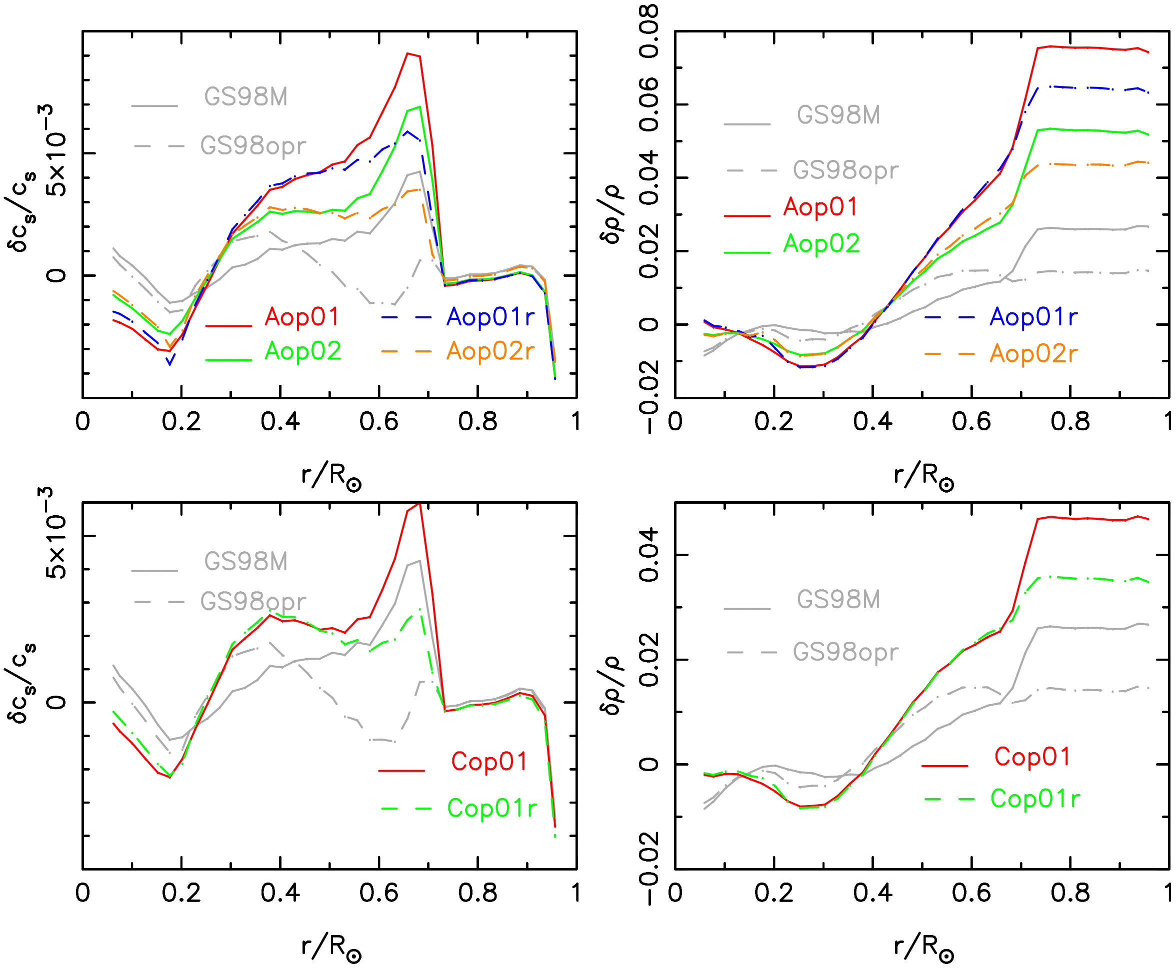

Figure 5. Relative sound-speed and density differences, in the sense (Sun-Model)/Model, between the Sun and models. The solar sound speed and density are given in Basu et al. (2009).

The gravitational settling and diffusion reduce the surface helium abundance of SSMs by around 11% (~ 0.03 by mass fraction) below its initial value (see Table 1), which plays an important role in shaping the sound-speed and density profiles of the models. Rotational mixing reduces the amount of the surface helium settling by about $33\%-36\%$. In order to counteract the effects of rotational mixing on the settling of elements, we increased the rates of element diffusion and settling by 36%, and then constructed rotating models Aop12r and Aopal12r by using OP and OPAL opacity tables. The two models had the surface heavy-element abundance determined by Lodders (2020). Tables 1 and 2 list their fundamental parameters and neutrino fluxes, respectively.

The sound-speed and density profiles of Aopal12r are almost as good as those of GS98M, but those of Aop12r are obviously better than those of GS98M (see Figure 7). The inferred CZ depth and observed frequency separation ratios r_{02} and r_{13} are reproduced well by the two models (see Table 1 and Figure 7). The total fluxes of ^{13}N, ^{15}O, and ^{17}F neutrinos are $\Phi(\mathrm{CNO}) = 8.37 \times 10^8$ cm^{-2} s^{-1} for Aop12r and $\Phi(\mathrm{CNO}) = 8.53 \times 10^8$ cm^{-2} s^{-1} for Aopal12r, which are consistent with the detected value of $7^{+3}_{-2} \times 10^8$ cm^{-2} s^{-1} (Borexino Collaboration 2020). However, the ^{8}B neutrino fluxes computed from Aop12r and Aopal12r are lower than that detected by Borexino Collaboration (2018) (see Table 2). The surface helium abundances of Aop12r and Aopal12r are 0.2413 and

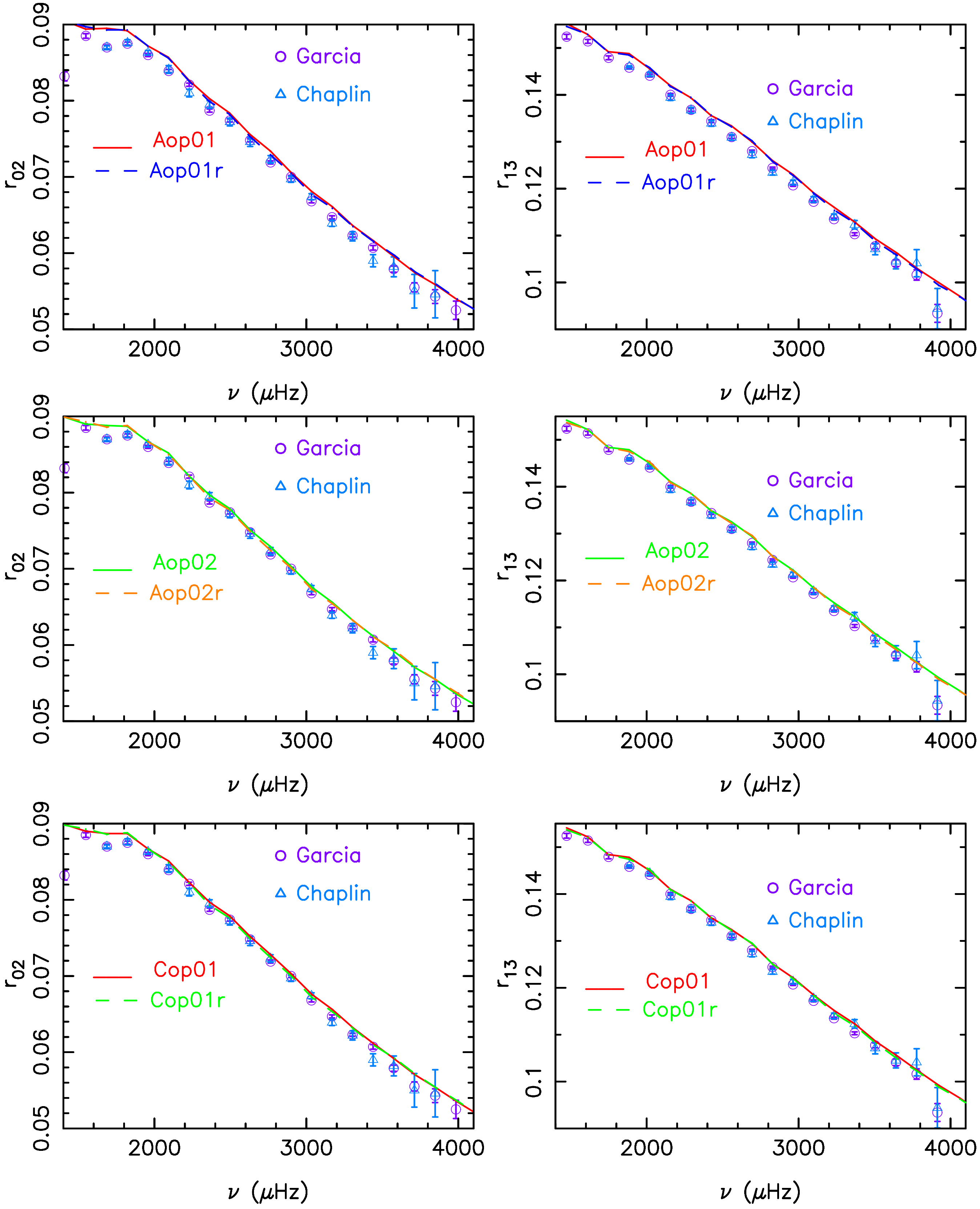

Figure 6. Distributions of observed and predicted ratios r_{02} and r_{13} as a function of frequency. The circles and triangles show the ratios calculated from the frequencies observed by GOLF & VIRGO (García et al. 2011) and BiSON (Chaplin et al. 1999), respectively.

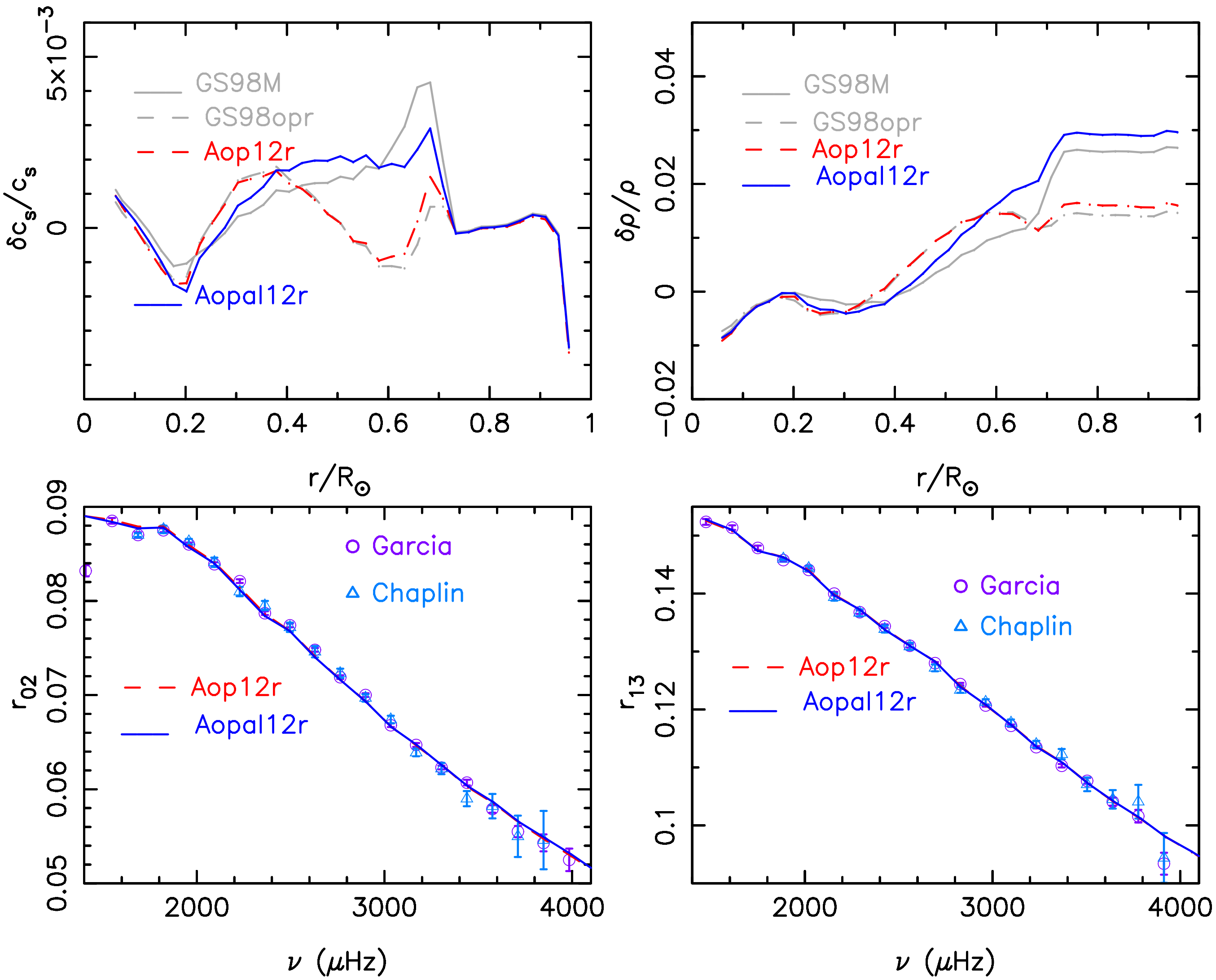

Figure 7. Top panels: relative sound-speed and density differences, in the sense (Sun-Model)/Model, between the Sun and models. The solar sound speed and density are given in Basu et al. (2009). Bottom panels: distributions of observed and predicted ratios r_{02} and r_{13} as a function of frequency. The circles and triangles show the ratios calculated from the frequencies observed by GOLF & VIRGO (García et al. 2011) and BiSON (Chaplin et al. 1999), respectively.

0.2424, respectively, which are consistent with 0.2423 ± 0.0054 advocated by Asplund et al. (2021) but lower than 0.2485 ± 0.0035 inferred by Basu & Antia (2004). Thus these models also do not completely agree with helioseismic results and updated neutrino fluxes.

3.2.3. *Rotating and Enhanced Diffusion Models Constructed in Accordance with Caffau Mixtures*

By using OPAL and OP opacity tables reconstructed with Caffau et al. (2011) mixtures, we computed rotating models Copal11r and Cop11r. In order to counteract the effects of rotational mixing on the settling of elements, same as the cases in models Aopal12r and Aop12r, the rates of element diffusion and settling were also increased by 36% in models Copal11r and Cop11r. The surface heavy-element abundance of 0.01548 for Copal11r is consistent with that determined by Caffau et al. (2010). Figure 8 shows that Copal11r has better sound-speed and density profiles (smaller $\chi^2_{c_s+\rho}$) than GS98M and reproduces the observed frequency separation ratios r_{02} and r_{13}. The relative differences $\delta c_s/c_s$ and $\delta\rho/\rho$ between the Sun and Copal11r are smaller than 0.0021 and 0.025, respectively. It also reproduces the seismically inferred surface helium abundance and radius r_{cz} at the level of 1σ (see Table 1).

The fluxes of *pp*, *pep*, *hep*, ^{7}Be, and ^{8}B neutrinos and the total fluxes of ^{13}N, ^{15}O, and ^{17}F neutrinos calculated from Copal11r are in agreement with those detected by Borexino Collaboration (2018, 2020) at the level of 1σ. The ^{8}B neutrino flux of 5.41×10^6 cm^{-2} s^{-1} is also in good agreement with $(5.21 \pm 0.27) \times 10^6$ cm^{-2} s^{-1} (Ahmed et al. 2004) but larger than that determined by Bergström et al. (2016) (see Table 2). Copal11r not only is in agreement with updated neutrino fluxes but has better sound-speed and density profiles than GS98M (see Figure 8 or Table 4). It is thus better than GS98M.

The surface heavy-element abundance of Cop11r is also 0.01548. Cop11r has better sound-speed and density profiles (smaller $\chi^2_{c_s+\rho}$) than Copal11r (see Figure 8 and Table 4). It also reproduces the observed r_{02} and r_{13}, inferred radius r_{cz}, and updated neutrino fluxes except the ^{8}B neutrino flux. The ^{8}B neutrino flux of Cop11r is 5.16×10^6 cm^{-2} s^{-1}, which is lower than $5.68^{+0.39}_{-0.41} \times 10^6$ cm^{-2} s^{-1} (Borexino Collaboration 2018) but in good agreement with that determined by Bergström et al. (2016). The surface helium abundance of 0.2431 for Cop11r is lower than 0.2485 ± 0.0035 inferred by Basu & Antia (2004) but consistent with 0.2423 ± 0.0054 advocated by Asplund et al. (2021). OP significantly improves the sound-speed and density profiles, but leads to the fact that the ^{8}B neutrino flux and surface helium abundance are lower than the inferred values. However, if $\Phi(^8\mathrm{B}) = 5.16^{+0.13}_{-0.09} \times 10^6$ cm^{-2} s^{-1} (Bergström et al. 2016) and $Y_s = 0.2423 \pm 0.0054$ (Asplund et al. 2021) are adopted, the $\Phi(^8\mathrm{B})$ and Y_s of GS98op are more consistent with these values than those of GS98M. In this case, GS98op is the best SSM with high metal abundances rather than GS98M; and Cop11r is better than GS98op.

Models Cop11r and Copal11r have the same input physics except opacity tables. The models constructed with OP opacity tables have better sound-speed and density profiles but lower surface helium abundance and ^{8}B neutrino flux than those constructed with OPAL opacity tables. The differences in the sound-speed and density profiles, surface helium abundances, and ^{8}B neutrino fluxes caused by the discrepancies in the opacities are marked. The results indicate that a small discrepancy in opacities can obviously affect the solar model.

3.3. *Possible Problems in Opacities*

In order to understand the effects of the differences in opacities on models, we constructed model Aop12ri with OP opacity tables and Co-

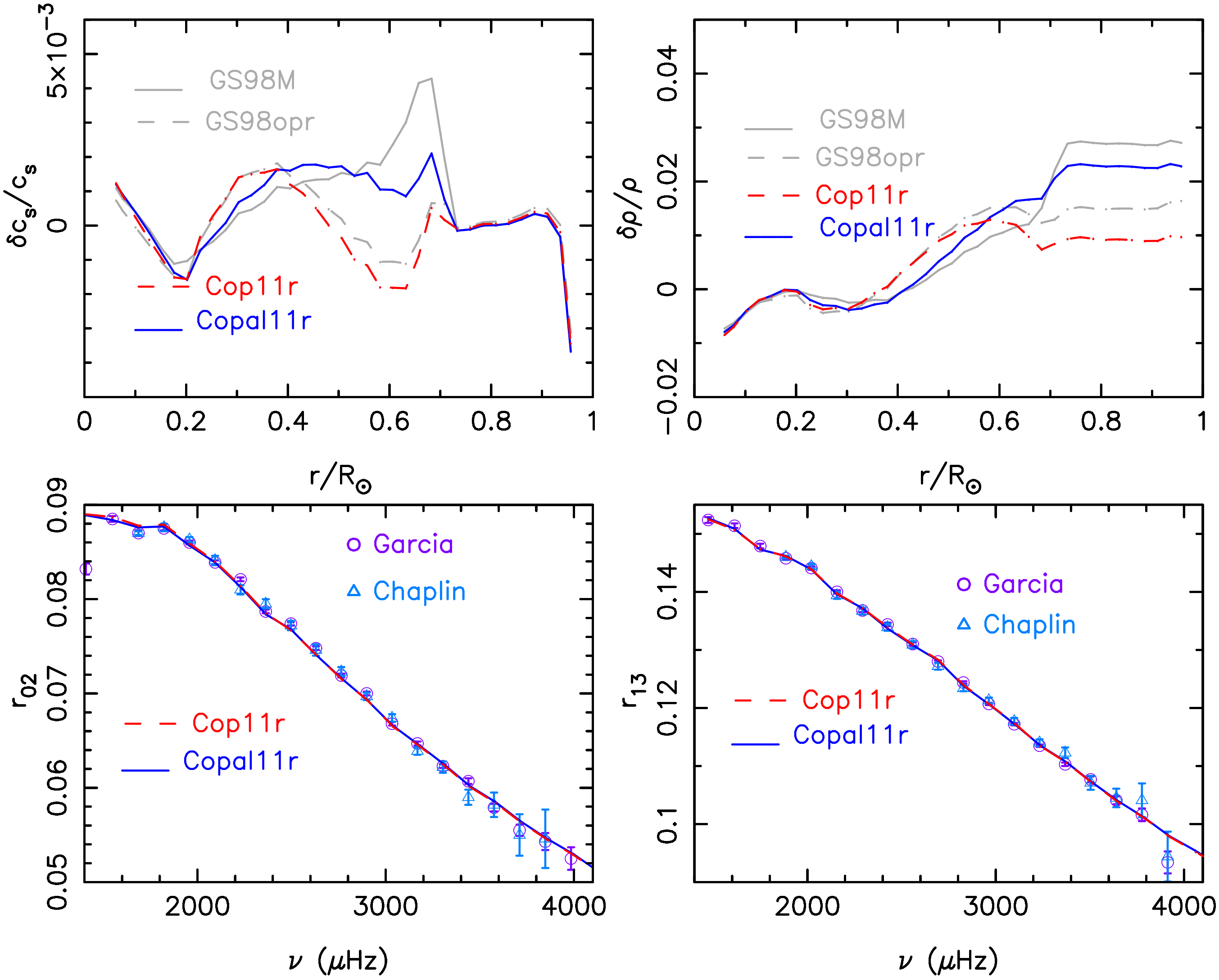

Figure 8. Top panels: relative sound-speed and density differences, in the sense (Sun-Model)/Model, between the Sun and models. The solar sound speed and density are given in Basu et al. (2009). Bottom panels: distributions of observed and predicted ratios r_{02} and r_{13} as a function of frequency. The circles and triangles show the ratios calculated from the frequencies observed by GOLF & VIRGO (García et al. 2011) and BiSON (Chaplin et al. 1999), respectively.

pal11ri with OPAL opacity tables. The OP opacities in the regions of Aop12ri with $T \gtrsim 4.5 \times 10^6$ K ($r \lesssim 0.45\ R_\odot$) were increased by about 1.5% ($k_0 \leq 1.015$, see Appendix A) to approximately match OPAL opacities in the same regions. The OPAL opacities for the regions of Copal11ri with 2×10^6 K $\lesssim T \lesssim 5 \times 10^6$ K were increased by about $1 - 2.3\%$ ($k_0 \leq 1.023$) to roughly match OP opacities (see Figure 9). The fundamental parameters and neutrino fluxes of these two models are also listed in Tables 1 and 2, respectively.

Aop12ri is in good agreement with helioseismic results and updated neutrino fluxes except the surface helium abundance and ^{8}B neutrino flux. The surface helium abundance of Aop12ri is 0.2436, which is lower than the seismically inferred value of 0.2485 ± 0.035. Moreover, the ^{8}B neutrino flux of Aop12ri is 5.19×10^6 cm^{-2} s^{-1}, which is lower than that detected by Borexino Collaboration (2018). But they are

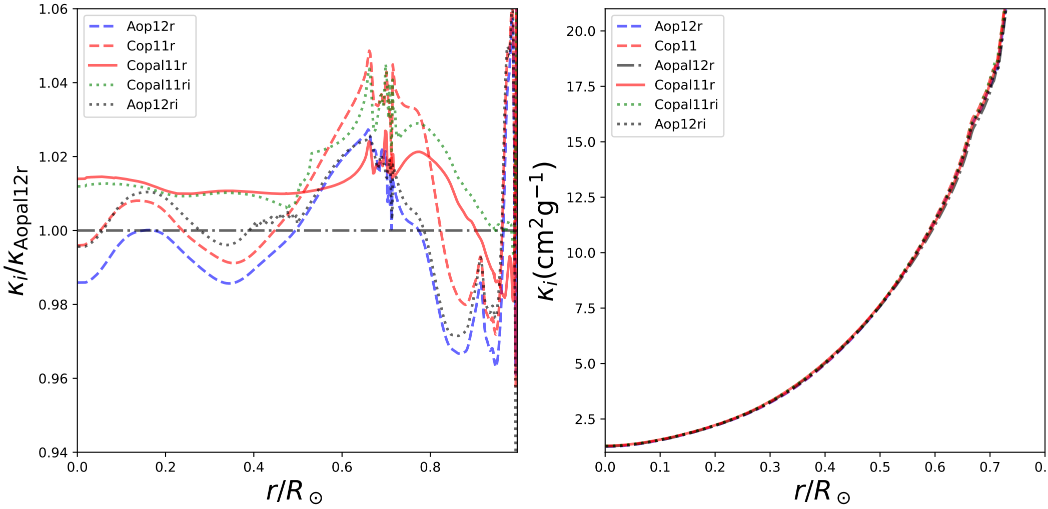

Figure 9. Left panel: comparison of Rosseland mean opacity of different models relative to that of Aopal12r. Right panel: distributions of Rosseland mean opacity of the models as a function of radius.

higher than those of Aop12r. The increase in OP opacities mainly improves the predictions of surface helium abundance and ^{8}B neutrino flux but slightly worsens the sound-speed and density profiles in comparison to those of Aop12r (see Table 4 or Figures 8 and 10). However, the sound-speed and density profiles of Aop12ri are still better than those of GS98M.

The increase in OPAL opacities has almost no effect on surface helium abundance and neutrino fluxes (see Table 2) but significantly improves the sound-speed and density profiles (see Figure 10). The relative differences $\delta c_s/c_s$ and $\delta\rho/\rho$ between Sun and Copal11ri are smaller than 0.00117 and 0.0178 near the BCZ, decreased by about 46% and 29% in comparison to those of Copal11r, respectively. Copal11ri reproduces the observed ratios r_{02} and r_{13} (see Figure 10) and the inferred helium abundance and r_{cz} at the level of 1σ. The neutrino fluxes calculated from Copal11ri also agree with those detected by Borexino Collaboration (2018, 2020) at the level of 1σ. Copal11ri is the best rotating model for the heavy-element abundance determined by Caffau et al. (2010). It is better than Copal11r and in good agreement with helioseismic results and updated neutrino fluxes.

The increase in OPAL opacities works well. The changes in OP opacities would have the same effect. In order to test this case, we constructed model Cop11ri. The OP opacities for the regions of Cop11ri with $T \gtrsim 4.5 \times 10^6$ K were increased by about 1.5% to approximately match OPAL opacities in the same regions. The calculations show that models Cop11ri and Copal11ri have almost the same sound-speed and density profiles (see Figure 10), surface helium and heavy-element abundances (see Table 1), and neutrino fluxes (see Table 2). They also have almost the same Z_0, Y_0, and $\alpha_{\rm MLT}$. The modified OP and OPAL opacities produce almost the same rotating models. These imply that the differences between Cop11r and Copal11r result from discrepancies in opacities, and that OPAL might underestimate opacities for the regions of the Sun with 2×10^6 K $\lesssim T \lesssim 5 \times 10^6$ K by about $1-2$%, or that OP might underestimate opacities in the regions of the Sun with $T \gtrsim 4.5 \times 10^6$ K by around 1.5%. The possible underestimate in OP leads to the fact that the models constructed with

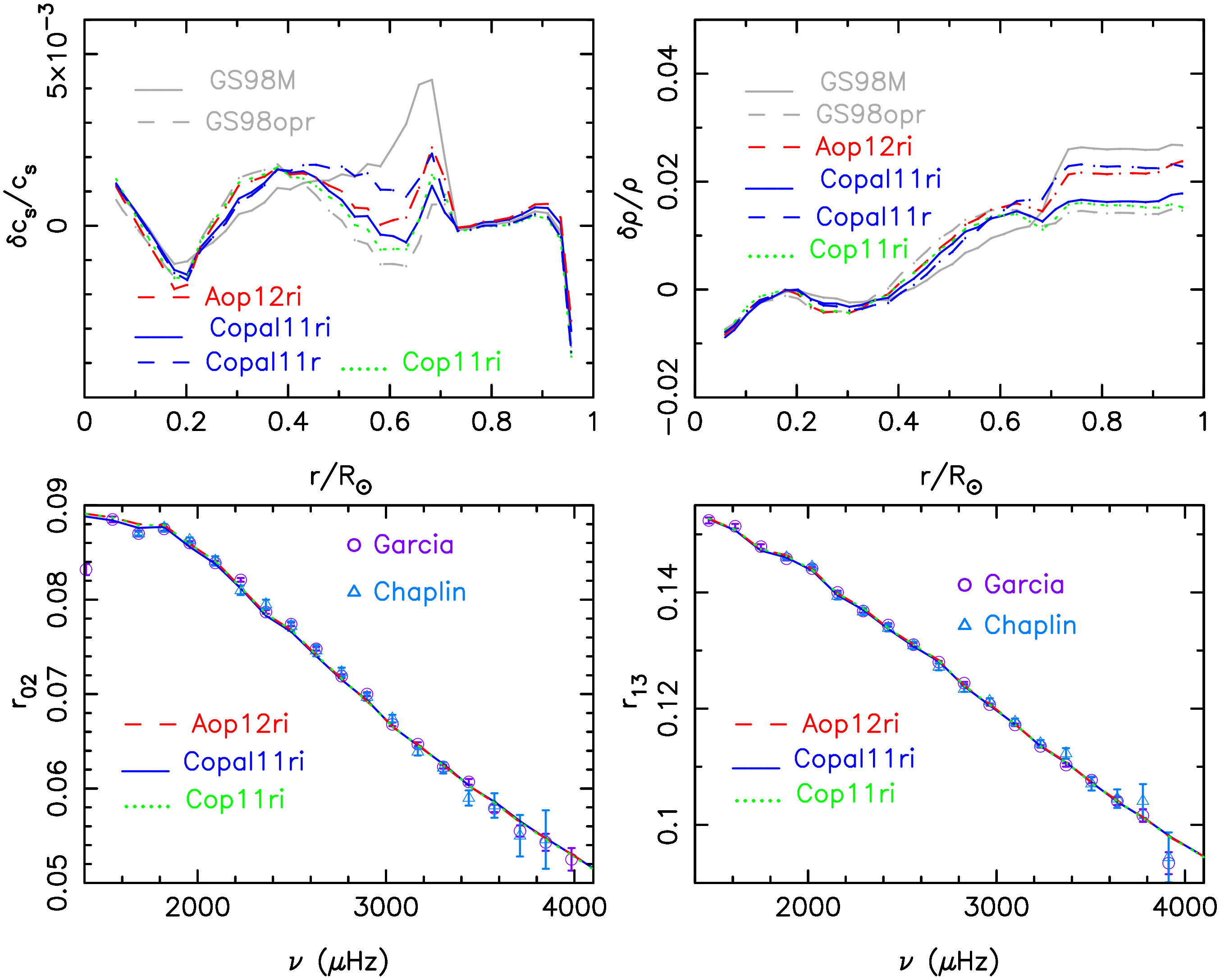

Figure 10. Top panels: relative sound-speed and density differences, in the sense (Sun-Model)/Model, between the Sun and models. The solar sound speed and density are given in Basu et al. (2009). Bottom panels: distributions of observed and predicted ratios r_{02} and r_{13} as a function of frequency. The circles and triangles show the ratios calculated from the frequencies observed by GOLF & VIRGO (García et al. 2011) and BiSON (Chaplin et al. 1999), respectively.

OP opacity tables have a lower surface helium abundance and ^{8}B neutrino flux than those constructed with OPAL opacity tables, while the possible underestimate in OPAL results in the fact that the sound-speed and density profiles of the models constructed with OPAL opacity tables are not as good as those of the models constructed with OP opacity tables.

With the modified opacities, only the models with the metal abundance determined by Lodders (2020) agree with the ^{8}B neutrino flux determined by Bergström et al. (2016) and the helium abundance advocated by Asplund et al. (2021), but the models with the metal abundance determined by Caffau et al. (2010) are in agreement with the ^{8}B neutrino flux detected by Borexino Collaboration (2018) and the seismically inferred helium abundance. Thus precisely determining ^{8}B neutrino flux aids in solving the solar abundance problem.

4. DISCUSSION AND SUMMARY

Although GS98M was chosen as the best SSM with high metal abundances, the value of Φ(CNO) of GS98M is slightly larger than the detected value of $7^{+3}_{-2} \times 10^8$ cm^{-2} s^{-1} (Borexino Collaboration 2020). That of GS98opr is in agreement with the detected one, but its ^{8}B neutrino flux is lower than that updated by Borexino Collaboration (2018). Thus the updated neutrino fluxes do not favour the high-Z models. Moreover, the values of Φ(CNO) calculated from the models with the heavy-element abundance determined by Asplund et al. (2021) are consistent with the detected value, but the ^{7}Be and ^{8}B neutrino fluxes predicted by the models are much lower than those determined by Bergström et al. (2016) and ones detected by Borexino Collaboration (2018). Therefore, the updated neutrino fluxes also do not prefer the models with the heavy-element abundance determined by Asplund et al. (2021). For the same input physics, the fluxes of ^{7}Be, ^{8}B, ^{13}N, ^{15}O, and ^{17}F neutrinos predicted by models increase with an increase in metallicity. These imply that the updated neutrino fluxes prefer a heavy-element abundance between that determined by GS98 and one advocated by Asplund et al. (2021).

Convection was treated according to the standard mixing-length theory (Böhm-Vitense 1958) in this work. The treatment of convection is one of the sources of uncertainty in modeling of stars. Different treatments of convection, such as Joyce & Chaboyer (2018), Spada et al. (2018, 2019), and Jermyn et al. (2022), could affect solar models and deserve more detailed study.

There are many $T-\tau$ relations for solar atmosphere (Krishna Swamy 1966; Ball 2022). The temperature, T reaches T_{eff} at $\tau = 2/3$ for the Eddington approximation but $\tau = 0.312156330$ for the Krishna Swamy (1966) $T-\tau$ relation, i.e. the solar radius R is defined at an outer layer for the Krishna Swamy (1966) $T-\tau$ relation. As a consequence, the Krishna Swamy (1966) $T-\tau$ relation requires a larger α_{MLT} to reproduce solar radius than the Eddington approximation (Demarque et al. 2008; Joyce & Chaboyer 2018; Spada et al. 2018). In order to study the effect of the $T-\tau$ relation on our results, we computed the solar models with the Eddington approximation. The calculations show that the $T-\tau$ relation has hardly any influence on neutrino fluxes, frequency separation ratios, and sound-speed and density profiles in the radiative region, but slightly affects the sound-speed and density profiles in the CZ (lead to a slight increase in $\chi^2_{c_s+\rho}$). Choosing between the Eddington approximation or Krishna Swamy (1966) $T-\tau$ relation does not change our results.

Rotational mixing can more efficiently inhibit the settling of helium than of heavy-element abundances because the mixing depends on the gradient of elements (Yang 2019). It can reduce the amount of the surface helium settling by about $33-36\%$ in our models, which is consistent with the result of Proffitt & Michaud (1991), who found that macroscopic turbulent mixing can reduce the amount of the surface helium settling by around 40%. It leads to the fact that the surface helium abundances of rotating models are obviously higher than those of non-rotating models. In the enhanced diffusion models, the velocity of diffusion and settling was increased by 36%. However, we have no obvious physical justification for the multiplier. In non-rotating models, the enhanced diffusion leaves the surface helium abundance too low. However, rotational mixing completely counteracts the effect of the enhanced diffusion on the surface helium abundance in rotating models. Thus the surface helium abundances of the rotating models with the enhanced diffusion are higher than those of non-rotating models. The effects of rotation and enhanced diffusion bring low-Z models into agreement with helioseismic results (Basu & Antia 2004; Basu et al. 2009) and updated neutrino fluxes (Borexino Collaboration 2018, 2020). However, the calculations show that the same effects can not bring high-Z models into agreement with the helioseismic results and the updated neutrino fluxes at the same time.

The effects of rotation and enhanced diffusion were studied by Yang (2019), where the value of multiplier (f_0) was larger than or equal to 1.5 and OPAL opacity tables constructed in accordance with AGSS09 mixtures were used. The flux of ^{7}Be neutrino and the total fluxes of ^{13}N, ^{15}O, and ^{17}F neutrinos predicted by the best model of Yang (2019) are larger than those detected by Borexino Collaboration (2018, 2020). The ^{7}Be neutrino flux is also higher than that determined by Bergström et al. (2016). Different from the earlier models of Yang (2019), Copal11r and Copal11ri, in which the value of multiplier is 1.36 and opacity tables are reconstructed in accordance with Caffau et al. (2011) mixtures, are in good agreement with the detected neutrino fluxes at the level of 1σ.

The differences between OPAL and OP opacities are small but can obviously affect the properties of solar models. The ^{8}B neutrino fluxes computed from models constructed with OP opacity tables are lower than those calculated from models constructed with OPAL opacity tables, which derives from the fact that OP underestimates opacities for the regions of the Sun with $T \gtrsim 5 \times 10^6$ K by about 1.5% compared to OPAL, especially in the core. As a consequence, the models constructed with OP opacity tables disagree with the ^{8}B neutrino flux detected by Borexino Collaboration (2018) but can agree with that determined by Bergström et al. (2016). Thus precisely determining the ^{8}B neutrino flux aid in diagnosing the opacities in the solar core.

Moreover, the sound-speed and density profiles of models constructed with OPAL opacity tables are obviously not as good as those of models constructed with OP opacity tables, which results from the fact that OPAL underestimates opacities for the regions of the Sun with 2×10^6 K $\lesssim T \lesssim 5 \times 10^6$ K by about $1-2\%$ compared to OP. If OPAL opacities in the regions are increased by about $1-2\%$ to approximately match OP opacities for the same regions, the models constructed with the OPAL opacities will produce better sound-speed and density profiles. If OP opacities for the regions of the Sun with $T \gtrsim 5 \times 10^6$ K are increased by about 1.5%, the model constructed with the OP opacities will be almost the same as that constructed with the modified OPAL opacities. These imply that the discrepancies between the sound speed and density of the Sun and those of the models could partly derive from opacity. The small differences between OPAL and OP opacities can obviously affect sound-speed and density profiles, surface helium abundance, and neutrino fluxes of models, which do not depend on mixture patterns. But the effect on neutrino fluxes slightly relies on the value of Z_0. In order to improve the solar model, the discrepancies between OPAL and OP may deserve more studies.

In this work, by using OP and OPAL opacity tables reconstructed with AAG21 and Caffau's mixtures, we constructed rotating solar models in which the effects of convection overshoot and enhanced diffusion were included. We obtained a rotating model, Copal11r, that is better than the SSM GS98M and the earlier rotating models of Yang (2016, 2019). The surface heavy-element abundance of Copal11r is 0.01548, which is consistent with the value of 0.0154 determined by Caffau et al. (2010) and that inferred by Basu & Antia (2004). The surface helium abundance of 0.2450 and the radius of the BCZ of 0.714 $R_\odot$ are in agreement with the seismically inferred values at the level of 1σ. The initial helium abundance is 0.2718, which is consistent with the value of 0.273 ± 0.006 inferred by Serenelli & Basu (2010). The ratios r_{02} and r_{13} of Copal11r agree with those calculated from observed frequencies. The sound-speed and density profiles of Copal11r are better than those of GS98M. Moreover, the fluxes of *pp*, *pep*, *hep*, ^{7}Be, and ^{8}B neutrinos and the total fluxes of ^{13}N, ^{15}O, and ^{17}F neutrinos calculated from Copal11r agree with those detected by Borexino Collaboration (2018, 2020) at the level of 1σ. The fluxes of ^{7}Be and ^{8}B neutrinos are also consistent with those determined by Bellini et al. (2011) and Ahmed et al. (2004). To recover the seismically inferred depth of the CZ, a convection overshoot of $\delta_{\rm ov} \approx 0.1$ is required in rotating models. Rotation or enhanced diffusion alone can improve sound-speed and density profiles, but the combination of rotation and enhanced diffusion is required to bring the rotating model into agreement with seismically inferred results and detected neutrino fluxes. More details of Copal11r are given in Appendix C.

If the surface helium abundance of 0.2423 ± 0.0054 advocated by Asplund et al. (2021) and the ^{8}B neutrino flux determined by Bergström et al. (2016) are adopted, we can obtain another rotating model, Cop11r, that is better than GS98op. The models constructed with OP opacity tables have obviously better sound-speed and density profiles but lower surface helium abundance and ^{7}Be, ^{8}B, ^{13}N, ^{15}O, and ^{17}F neutrino fluxes than those constructed with OPAL opacity tables. The calculations show that OPAL may underestimate opacities for the regions of the Sun with 2×10^{6} K $\lesssim T \lesssim 5 \times 10^{6}$ K by about $1 - 2\%$, and that OP may underestimate opacities in the regions of the Sun with $T \gtrsim 5 \times 10^{6}$ K by around 1.5%. If the possible underestimate of OPAL or OP were corrected, the model better than Copal11r or Cop11r would be obtained.

The author thanks the anonymous referee for helpful comments that helped the author improve this work, as well as Dr Xianfei Zhang and Tanda Li for their help, and acknowledges the support from the NSFC 11773005 and U1631236.

REFERENCES

Adelberger, E. G., et al. 1998, Rev. Mod. Phys., 70, 1265
Adelberger E. G., et al. 2011, RMP, 83, 195
Ahmed, S. N., Anthony, A. E., Beier, E. W. et al. 2004, PhRvL, 92, 1301
Amarsi, A. M., Grevesse, N., Asplund, M., Collet, R. 2021, A&A, 656, 113
Antia, H. M., & Basu, S. 2006, ApJ, 644, 1292
Asplund, M., Amarsi, A. M., Grevesse, N. 2021, A&A 653, A141
Asplund, M., Grevesesse N., Sauval, A. J., Allende Prieto, C., & Kiselman, D. 2004, A&A, 417, 751
Asplund, M., Grevesesse, N., Sauval, A. J., Allende Prieto, C., & Blomme, R. 2005, A&A, 431, 693
Asplund, M., Grevesse, N., Sauval, A., & Scott, P. 2009, ARA&A, 47, 481 (AGSS09)
Baby, L. T., et al. 2003a, Phys. Rev. Lett., 90, 022501
Badnell, N. R., Bautista, M. A., Butler, K., Delahaye, F., Mendoza, C., Palmeri, P., Zeippen, C. J., Seaton, M. J. 2005, MNRAS, 360, 458
Bahcall, J. N. , 1989, Neutrino Astrophysics (Cambridge University, Cambridge, England).
Bahcall, J. N., Pinsonneault, M. H., & Basu, S, 2001, ApJ, 555, 990
Bahcall, J. N., & Pinsonneault, M. H. 1992, Rev. Mod. Phys., 64, 885 (BP92)
Bahcall J. N., Pinsonneault M. H., & Wasserburg G. J. 1995, Rev. Mod. Phys., 67, 781
Bahcall, J. N., Basu, S., Pinsonneault, M. H., & Serenelli, A. M. 2005, ApJ, 618, 1049

Bahcall, J. N., & Pinsonneault, M. H. 2004, Phys. Rev. Lett., 92, 121301 (BP04)

Bahcall, J. N., Serenelli, A. M., & Pinsonneault, M. H. 2004, ApJ, 614, 464

Bahcall, J. N., & Ulrich, R. 1988, RvMP, 60, 297

Ball, W. H. 2021, RNAAS, 5, 7

Basu, S., & Antia, H. M. 1997, MNRAS, 287, 189

Basu, S., & Antia, H. M. 2004, ApJL, 606, L85

Basu, S., Chaplin, W. J., Elsworth, Y., New, R., & Serenelli, A. M. 2009, ApJ, 699, 1403

Basu, S., Grevesse, N., Mathis, S., Turck-Chièze, S. 2015, Space Sci Rev., 196, 49

Basu, S., Pinsonneault, M. H., & Bahcall, J. N. 2000, ApJ, 529, 1084

Bellini, G. Benziger, J. Bick, D. et al. 2011, PhRvL, 107, 141302

Bellini, G. Benziger, J. Bick, D. et al. 2012, PhRvL, 108, 51302

Bergström, J., Gonzalez-Garcia, M. C., Maltoni, M., et al. 2016, JHEP, 3, 132

Böhm-Vitense, E. 1958, ZAp, 46, 108

Borexino Collaboration, Agostini, M., Altenmüller, K., et al. 2018, Nature, 562, 505

Borexino Collaboration, Agostini, M., Altenmüller, K., Appel, S., et al. 2020, Nature, 587, 577

Buldgen, G.,Salmon, S. J. A. J., Noels, A., Scuflaire, R., Dupret, M. A., Reese, D. R. 2017, MNRAS, 472, 751

Buldgen, G., Salmon, S. J. A. J., Noels, A., et al. 2019, A&A, 621, 33

Caffau, E., Ludwig, H.-G., Bonifacio, P., Faraggiana, R., Steffen, M., Freytag, B., Kamp, I., Ayres, T. R. 2010, A&A, 514, A92

Caffau, E., Ludwig, H.-G., Steffen, M., Freytag, B., Bonifacio, P. 2011, Solar Phys., 268, 255

Castro, M., Vauclair, S., & Richard, O. 2007, A&A, 463, 755

Chaboyer, B., Demarque, P., Pinsonneault, M. H. 1995, ApJ, 441, 865

Chaplin, W. J., Elsworth, Y., Howe, R., et al. 1996, Sol. Phys., 168, 1

Chaplin, W. J., Elsworth, Y., Isaak, G. R., Miller, B. A., & New, R. 1999b, MNRAS, 308, 424

Christensen-Dalsgaard, J., Gough, D. O., & Thompson, M. J. 1991, ApJ, 378, 413

Christensen-Dalsgaard, J. 2021, Living Reviews in Solar Physics, 18, 2

Delahaye, F., Zwölf, C. M., Zeippen, C. J., Mendoza, C. 2016, JQSRT, 171, 66

Demarque, P., Guenther, D. B., Li, L. H., Mazumdar, A., Straka, C. W. 2008, Ap&SS, 316, 31

Endal, A. S., & Sofia, S. 1978, ApJ, 220, 279

Ferguson, J. W., Alexander, D. R., Allard, F. et al. 2005, ApJ, 623, 585

García, R. A., Salabert, D., & Ballot, J. et al. 2011, JPhCS, 271, 2049

Grevesse, N., & Sauval, A. J. 1998, in Solar Composition and Its Evolution, ed. C. Fröhlich et al. (Dordrecht: Kluwer), 161 (GS98)

Guenther D. B., 1994, ApJ, 422, 400

Guzik, J. A., Watson, L. S. & Cox, A. N. 2005, ApJ, 627, 1049

Guzik, J. A., & Mussack, K. 2010, ApJ, 713, 1108

Hope, C., Bergemann, M., Bitsch, B., Serenelli, A. 2020, A&A, 641, A73

Iglesias, C., Rogers, F. J. 1996, ApJ, 464, 943

Jermyn, A. S., Anders, E. H., Lecoanet, D. & Cantiello, M. 2022, arXiv220600011

Joyce, M., & Chaboyer, B. 2018, ApJ, 864, 99

Junghans, A. R., et al. 2003, Phys. Rev. C, 68, 065803

Kawaler, S. D. 1988, ApJ, 333, 236

Kippenhahn, R., Weigert, A., & Weiss, A. 2012, Stellar Structure and Evolution, (Heidelberg: Springer)

Krishna Swamy, K. S. 1966, ApJ, 145, 174

Le Pennec, M., Turck-Chièze, S., Salmon, S., Blancard, C., Cossé, P., Faussurier, G., Mondet, G. 2015, ApJL, 813, L42

Lodders, K. 2003, ApJ, 591, 1220

Lodders, K., Palme, H., Gail, H-P. 2009, LanB, 4, 712 (LPG09)

Lodders, K. 2020, Solar Elemental Abundances, in The Oxford Research Encyclopedia of Planetary Science, Oxford University Press, arXiv:1912.00844

Marcucci, L. E., Schiavilla, R., Viviani, M., Kievski, A., & Rosati, S. 2000, PhRvL, 84, 5959

Montalbán, J., Miglio, A., Noels, A., Grevesse, N., Di Mauro, M. P. 2004, in Helio- and Asteroseismology: Towards a Golden Future, Proc. of the SOHO 14 / GONG 2004 Workshop, ed. D. Danesy (ESA SP-559; Noordwijk: ESA), 574

Montalbán, J., Miglio, A., Theado, S., Noels, A., Grevesse, N. 2006, Commun. Asteroseismol., 147, 80

Pinsonneault, M. H., Kawaler, S. D., Sofia, S., & Demarqure, P. 1989, ApJ, 338, 424

Proffitt, C. R., & Michaud, G. 1991, ApJ, 380, 238

Rogers, F., & Nayfonov, A. 2002, ApJ, 576, 1064

Roxburgh, I. W., & Vorontsov, S. V. 2003, A&A, 411, 215

Salmon, S.J.A.J., Buldgen, G., Noels, A., Eggenberger, P., Scuflaire, R., Meynet, G. 2021, A&A, 651, A106

Schiavilla, R., Wiringa, R. B., Pandharipande, V. R., and Carlson, J. 1992, Phys. Rev. C, 45, 2628

Schramm, D. N., & Shi, X. 1994, NuPhS, 35, 321

Seaton, M. J. 1987, JPhB, 20, 6363

Serenelli, A., & Basu, S. 2010, ApJ, 719, 865

Serenelli, A. M., Basu, S., Ferguson, J. W., & Asplund, M. 2009, ApJL, 705, L123

Serenelli, A., Haxton, W. C., Peña-Garay, C. 2011, ApJ, 743, 24

Schou, J., Antia, H. M., Basu, S. et al. 1998, ApJ, 505, 390

Spada, F., Demarque, P., Basu, S., Tanner, J. D. 2018, ApJ, 869, 135

Spada, F., & Demarque, P. 2019, MNRAS, 489, 4712

The Opacity Project Team, 1995, The Opacity Project Vol. 1, Institute of Physics Publications, Bristol, UK

Thoul, A. A., Bahcall, J. N., Loeb, A. 1994, ApJ, 421, 828

Turck-Chièze, S., & Couvidat, S. 2011, RPPh, 74, 6901

Turck-Chièze, S., Palacios, A., Marques, J. P., Nghiem, P. A. P. 2010, ApJ, 715, 1539

Turck-Chièze, S., Piau, L., & Couvidat, S. 2011, ApJL, 731, L29

Vorontsov, S. V., Baturin, V. A., Ayukov, S. V., Gryaznov, V. K. 2013, MNRAS, 430, 1636

Vorontsov, S. V., Baturin, V. A., Ayukov, S. V., Gryaznov, V. K. 2014, MNRAS, 441, 3296

Wolfs, F. L. H.,; Freedman, S. J., Nelson, J. E., Dewey, M. S., Greene, G. L. 1989, PhRvL, 63, 2721

Yang, W. 2016, ApJ, 829, 68

Yang, W., 2019, ApJ, 873, 18

Yang, W. M., & Bi, S. L. 2007, ApJL, 658, L67

Zhang, Q., & Li, Y. 2012, ApJ, 746, 50

Zhang, Q. S., Li, Y., Christensen-Dalsgaard, J. 2019, ApJ, 881, 103

Zahn, J. P. 1993, in Astrophysical Fluid Dynamics, Les Houches XLVII, ed. J.-P. Zahn & J. Zinn-Justin (New York: Elsevier), 561

Table 1. Fundamental Parameters of Solar Models Constructed in Accordance with Different Mixtures.

Model	Y_0	Z_0	$\alpha_{\rm MLT}$	$\delta_{\rm ov}$	f_0	ρ_c	r_{cz}	Y_s	Z_s	$(Z/X)_s$	ΔY	Ω_i
Opacity Tables Constructed with GS98 mixtures												
GS98M	0.2761	0.01940	2.1223	0	1.0	154.59	0.716	0.2455	0.0174	0.0237	0.0306	0
GS98Mr	0.2735	0.01896	2.0754	0.05	1.0	154.11	0.715	0.2534	0.0170	0.0234	0.0201	10
GS98op	0.2713	0.01894	2.1352	0	1.0	154.25	0.716	0.2414	0.0170	0.0230	0.0299	0
GS98opr	0.2711	0.01890	2.0979	0.05	1.0	154.16	0.714	0.2512	0.0170	0.0232	0.0199	10
Opacity Tables Constructed with AAG21 mixtures												
Aop01	0.2583	0.01557	2.0722	0	1.0	151.98	0.725	0.2283	0.0139	0.0184	0.0300	0
Aop02	0.2648	0.01661	2.0954	0	1.0	152.89	0.722	0.2347	0.0149	0.0199	0.0301	0
Aop01r	0.2582	0.01554	2.0383	0.15	1.0	151.86	0.716	0.2389	0.0140	0.0187	0.0193	10
Aop02r	0.2648	0.01659	2.0596	0.15	1.0	152.88	0.713	0.2453	0.0149	0.0202	0.0195	10
Aop12r	0.2675	0.01717	2.1055	0.10	1.36	154.42	0.714	0.2413	0.0149	0.0201	0.0262	10
Aopal12r	0.2690	0.01720	2.0872	0.10	1.36	154.27	0.714	0.2424	0.0149	0.0201	0.0266	10
Aop12ri	0.2702	0.01722	2.0918	0.10	1.36	154.34	0.715	0.2436	0.0149	0.0202	0.0266	10
Opacity Tables Constructed with Caffau mixtures												
Cop01	0.2666	0.01719	2.0924	0	1.0	152.87	0.720	0.2365	0.0154	0.0206	0.0301	0
Cop01r	0.2664	0.01714	2.0582	0.12	1.0	152.76	0.714	0.2467	0.0154	0.0209	0.0197	10
Cop11r	0.2695	0.01780	2.1056	0.10	1.36	154.42	0.711	0.2431	0.01548	0.0209	0.0264	10
Cop11ri	0.2717	0.01777	2.0883	0.10	1.36	154.29	0.714	0.2450	0.0154	0.0209	0.0267	10
Copal11r	0.2717	0.01784	2.0817	0.10	1.36	154.25	0.713	0.2450	0.01548	0.0209	0.0267	10
Copal11ri	0.2720	0.01774	2.0865	0.10	1.36	154.46	0.712	0.2453	0.0154	0.0209	0.0267	10

Note—The central density ρ_c, CZ radius r_{cz}, and initial angular velocity Ω_i are in units of g cm^{-3}, $R_\odot$, and 10^{-6} rad s^{-1}, respectively. The quantity $\Delta Y = Y_0 - Y_s$ is the amount of surface helium settling.

Table 2. Predicted and Measured Solar Neutrino Fluxes.

model	T_c	*pp*	*pep*	*hep*	^{7}Be	^{8}B	^{13}N	^{15}O	^{17}F
BP04	...	5.94	1.40	7.88	4.86	5.79	5.71	5.03	5.91
SSeM	...	5.92	1.39	....	4.85	4.98	5.77	4.97	3.08
Measured	...	$6.06^{+0.02}_{-0.06}$[a]	1.6±0.3[b]	...	4.84±0.24[a]	5.21±0.27[c]	...	...	...
B16[d]	...	$5.97^{+0.04}_{-0.03}$	1.448±0.013	19^{+12}_{-9}	$4.80^{+0.24}_{-0.22}$	$5.16^{+0.13}_{-0.09}$	≤13.7	≤2.8	≤85
Borexino[e]	...	6.1±0.5	1.39±0.19	<220	4.99±0.11	$5.68^{+0.39}_{-0.41}$	7^{+3}_{-2}		
GS98M	15.777	5.95	1.40	9.69	5.09	5.59	5.40	4.77	5.52
GS98Mr	15.733	5.96	1.41	9.73	4.95	5.29	5.08	4.45	5.14
GS98op	15.706	5.98	1.42	9.81	4.92	5.18	4.97	4.35	5.02
GS98opr	15.693	5.97	1.41	9.78	4.86	5.07	4.90	4.28	4.93
Aop01	15.513	6.05	1.45	10.19	4.42	4.12	3.43	2.91	3.32
Aop02	15.604	6.02	1.43	9.79	4.66	4.60	3.97	3.43	3.93
Aop01r	15.498	6.03	1.44	10.15	4.36	4.01	3.37	2.85	3.25
Aop02r	15.598	6.01	1.43	9.99	4.63	4.55	3.94	3.40	3.89
Aop12r	15.680	5.97	1.42	9.84	4.82	4.98	4.45	3.88	4.47
Aopal12r	15.706	5.97	1.42	9.81	4.87	5.09	4.54	3.96	4.57
Aop12ri	15.715	5.96	1.41	9.77	4.91	5.19	4.61	4.04	4.66
Cop01	15.645	6.00	1.42	9.95	4.75	4.82	4.25	3.69	4.24
Cop01r	15.623	5.98	1.42	9.92	4.66	4.65	4.16	3.59	4.12
Cop11r	15.716	5.95	1.41	9.77	4.89	5.16	4.73	4.15	4.79
Cop11ri	15.751	5.94	1.40	9.70	4.99	5.38	4.90	4.32	4.99
Copal11r	15.761	5.95	1.41	9.71	4.99	5.41	4.93	4.34	5.03
Copal11ri	15.764	5.95	1.41	9.72	5.00	5.44	4.92	4.34	5.02

NOTE—The table shows the predicted fluxes, in units of $10^{10}(pp)$, $10^9(^7\mathrm{Be})$, $10^8(pep, ^{13}\mathrm{N}, ^{15}\mathrm{O})$, $10^6(^8\mathrm{B}, ^{17}\mathrm{F})$, and $10^3(hep)$ cm^2 s^{-1}. The central temperature T_c of models is in unit of 10^6 K. The BP04 is the best model of Bahcall & Pinsonneault (2004) and has the GS98 mixtures. The SSeM is the best seismic model with high metal abundances that can reproduce inferred sound speed (Turck-Chièze & Couvidat 2011).

[a] Bellini et al. (2011).

[b] Bellini et al. (2012).

[c] Ahmed et al. (2004).

[d] Bergström et al. (2016).

[e] The total fluxes produced by CNO cycle are given in Borexino Collaboration (2020), other neutrino fluxes are given in Borexino Collaboration (2018).

Table 3. Physical Configurations of Models.

Model Name	Mixtures	Opacity	Enhanced Diffusion	Z_s value	Rotation	Increased Opacity (k_0)[a]
GS98M	GS98	OPAL	No	GS98	No	No
GS98Mr	GS98	OPAL	No	GS98	Yes	No
GS98op	GS98	OP	No	GS98	No	No
GS98opr	GS98	OP	No	GS98	Yes	No
Aop01	AAG21[b]	OP	No	AAG21	No	No
Aop02	AAG21	OP	No	Lodders 2020	No	No
Aop01r	AAG21	OP	No	AAG21	Yes	No
Aop02r	AAG21	OP	No	Lodders 2020	Yes	No
Aop12r	AAG21	OP	Yes	Lodders 2020	Yes	No
Aop12ri	AAG21	OP	Yes	Lodders 2020	Yes	Yes($1 \leq k_0 \leq 1.015$)
Aopal12r	AAG21	OPAL	Yes	Lodders 2020	Yes	No
Cop01	Caffau[c]	OP	No	Caffau	No	No
Cop01r	Caffau	OP	No	Caffau	Yes	No
Cop11r	Caffau	OP	Yes	Caffau	Yes	No
Cop11ri	Caffau	OP	Yes	Caffau	Yes	Yes($1 \leq k_0 \leq 1.015$)
Copal11r	Caffau	OPAL	Yes	Caffau	Yes	No
Copal11ri	Caffau	OPAL	Yes	Caffau	Yes	Yes($1 \leq k_0 \leq 1.023$)

NOTE—[a] See the Appendix A. [b]See the Table 5 in Appendix A and Asplund et al. (2021). [c]See the Table 5 and Caffau et al. (2010, 2011).

Table 4. The Values of χ^2 of Different Models.

Model	$\chi^{2\ a}_{c_s+\rho}$	$\chi^{2\ b}_{d02+13}$	$\chi^{2\ c}_{Borexino-neutrino}$	$\chi^{2\ d}_{\rm helium}$
GS98M	882.4	1.2	0.53	0.7
GS98Mr	799.2	1.4	0.49	2.0
GS98op	578.2	1.8	0.61	4.1
GS98opr	369.6	1.5	0.88	0.6
Aop01	6244.7	19.0	7.08	33.3
Aop02	3144.1	16.2	2.85	15.5
Aop01r	4424.0	9.0	8.43	7.5
Aop02r	1983.0	7.0	3.23	0.8
Aop12r	389.1	1.7	1.11	4.2
Aopal12r	917.4	1.6	0.78	3.0
Aop12ri	524.3	2.0	0.57	2.0
Cop01	2440.7	8.3	1.72	11.8
Cop01r	1402.2	6.5	2.75	0.3
Cop11r	323.7	1.6	0.67	2.4
Cop11ri	369.7	1.8	0.38	1.0
Copal11r	590.6	1.5	0.37	1.0
Copal11ri	342.6	1.6	0.35	0.8

NOTE—The function χ^2 defined as $\chi^2 = \frac{1}{N}\sum_{i=1}^{N}\frac{(q_{\rm ob,i}-q_{\rm th,i})^2}{\sigma_i^2}$, where $q_{\rm ob,i}$ and $q_{\rm th,i}$ are the observed/inferred and theoretical values of quantities $q_{\rm i}$, respectively; σ_i are the errors associated to the corresponding observed/inferred quantities; N is the number of the quantities.

[a] The inferred c_s and ρ are given in Basu et al. (2009).

[b] The observed d_{02} and d_{13} are calculated from the frequencies given by Chaplin et al. (1999).

[c] In order to calculate the value of $\chi^2_{\rm Borexino-neutrino}$, the $\Phi(hep) < 220 \times 10^3$ cm^2 s^{-1} of Borexino Collaboration (2018) was replaced by $\Phi(hep) = 19^{+12}_{-9} \times 10^3$ cm^2 s^{-1} of Bergström et al. (2016).

[d] The inferred helium is 0.2485 ± 0.0035 (Basu & Antia 2004).

APPENDIX

A. OPACITY TABLES

The low-temperature opacity tables with the mixtures listed in Table 5 were downloaded from https://www.wichita.edu/academics/fairmount_college_of_liberal_arts_and_sciences/physics/Research/opacity.php. The OPAL and OP opacity tables with the same mixtures were computed from https://opalopacity.llnl.gov/type1inp.html and http://op-opacity.obspm.fr/opacity/, respectively. The OP opacities did not consider the contributions of P, Cl, K, and Ti compared to OPAL opacities. The contributions of the missing elements (P, Cl, K, and Ti) were automatically transferred to other elements (see the note of the website of OP). The opacity tables, used in this work, are also available at the author's github repository at https://github.com/yangwuming/SUN.

The low-temperature opacity tables were used in the low-temperature region with $\lg T < 4.0$, and OPAL or OP tables were used in the high-temperature region with $\lg T > 4.1$. In the region with $4.0 \leq \lg T \leq 4.1$, the opacity was linearly interpolated between the high-temperature and low-temperature opacities. Moreover, we corrected the wrong CALL YALO2D in the subroutine YALO3D2 of YREC, which mainly affects the value of mixing-length parameter $\alpha_{\rm MLT}$ (lead to a small decrease in $\alpha_{\rm MLT}$). For models Aop12ri, Copal11ri, and Cop11ri, we applied a straight multiplier k_0 to opacity κ to enhance the opacity in a given region (see Section 3.3).

B. NUCLEAR REACTIONS

The nuclear reaction rates in conjunction with the corresponding energy release of three alternative *pp* branches ($pp1, pp2, pp3$), CNO cycle, and helium burning are calculated in YREC. The sequence of the reactions is explicitly listed in Demarque et al. (2008). The standard reaction rates implemented are identical to the rates published in Bahcall (1989). The calculated energy generation and neutrino fluxes are dependent on Q-values and nuclear cross-section factors S_0, respectively. The default Q-values are taken from the Table 21 of Bahcall & Ulrich (1988) and not changed. The default values of nuclear cross-section factors S_0 are taken from the Tables 3.2 and 3.4 of Bahcall (1989). Compared with the default and those adopted by Bahcall & Pinsonneault (1992), we adopted different $S_0(hep)$ and $S_0(^7\mathrm{Be} + \mathrm{p})$, which are shown in Table 6. The value of 0.0202 keV barns of $S_0(^7\mathrm{Be}+\mathrm{p})$ (Schramm & Shi 1994) is in agreement with 0.0205 ± 0.0007 keV barns of Baby et al. (2003) and 0.0208 ± 0.0007 keV barns of Adelberger et al. (2011). Moreover, if $S_0(hep) = 15.3 \times 10^{-20}$ keV barns (Wolfs et al. 1989) is adopted, the value of *hep* flux of model Copal11r is 14.4×10^3 cm^2 s^{-1}, which is in better agreement with that determined by Bergström et al. (2016). The changes in $S_0(hep)$ and $S_0(^7\mathrm{Be}{+}\mathrm{p})$ affect, respectively, only the *hep* and ^{8}B fluxes (Bahcall & Pinsonneault 2004). All models were computed by using the same Q-values and S_0.

C. NUMERICAL SOLAR MODEL AND DATA AVAILABILITY

Table 7 presents a basic numerical description of model Copal11r. All models and data used in this work are availabe at the author's github repository at https://github.com/yangwuming/SUN. In the old YREC, opacity was calculated by linearly interpolating between the opacity of a given Z_1 and that of another

Table 5. Fractional Abundances of Heavy Elements Used to Construct Opacity Tables.

Element	Number fraction (Caffau's mixtures)	Number fraction (AAG21 mixtures)
C	0.260408	0.266509
N	0.059656	0.062476
O	0.473865	0.452597
Ne	0.096751	0.106099
Na	0.001681	0.001534
Mg	0.029899	0.032788
Al	0.002487	0.002487
Si	0.029218	0.029903
P	0.000237	0.000238
S	0.011632	0.012182
Cl	0.000150	0.000189
Ar	0.002727	0.002217
K	0.000106	0.000109
Ca	0.001760	0.001844
Ti	0.000072	0.000086
Cr	0.000385	0.000385
Mn	0.000266	0.000243
Fe	0.027268	0.026651
Ni	0.001431	0.001465

NOTE—The number fraction of Caffau's mixtures were listed by Ferguson in the WSU low temperature opacities, while those of AAG21 mixtures were calculated by using the data in Table 2 of Asplund et al. (2021).

given Z_2 for heavy-element diffusion. We modified the code to linearly interpolate between a series of Z values (with $\delta Z = 0.001$) for the heavy-element diffusion. The amended YREC package, including pulsation code, are available from the author at yangwuming@bnu.edu.cn.

Table 6. Some of Nuclear Cross-section Factors S_0 (keV barns).

Reaction	Default^a	BP92	BP04	This work
^{1}H(p, e$^+\nu_e$) ^{2}H	4.07×10^{-22}	$4.00^{+0.06}_{-0.04} \times 10^{-22}$	$3.94(1 \pm 0.004) \times 10^{-22}$	4.00×10^{-22}
^{1}H($p + e^-$, ν_e) ^{2}H	Eq. (3.17)^a	Eq. (3.17)^a	Eq. (3.17)^a	Eq. (3.17)^a
^{3}He(^{3}He, 2p) ^{4}He	5.15×10^3	$5.00(1 \pm 0.06) \times 10^3$	5.4×10^3	5.00×10^3
^{3}He(^{4}He, γ) ^{7}Be	0.54	0.533(1 ± 0.032)	0.533	0.533
^{7}Be(e^-, ν_e) ^{7}Li	Eq. (3.18)^a	Eq. (3.18)^a	Eq. (26)^b	Eq. (3.18)^a
^{7}Be(p, γ) ^{8}B	0.0243	0.0224(1 ± 0.093)	0.0206±0.0008^c	0.0202^d
^{3}He(p, e$^+\nu_e$)^{4}He	8×10^{-20}	1.30×10^{-20}	$(8.6 \pm 1.3) \times 10^{-20}$	$2.30 \times 4.5^e \times 10^{-20}$

Note—[a] Bahcall (1989). [b] The equation of Adelberger et al. (1998). [c] $S_{20\ \mathrm{keV}}(^7\mathrm{Be}+\mathrm{p})$ given by Junghans et al. (2003). [d] The value given by Schramm & Shi (1994). [e] The value of $S_0(hep)$ given by Schiavilla et al. (1994) is 2.30×10^{-20}, which should be multiplied by a factor of 4.5 (Marcucci et al. 2000).

Table 7. Numerical Description of Model Copal11r.

$M/M_\odot$	$r/R_\odot$	$L/L_\odot$	T (K)	ρ (g cm^{-3})	p (dyn cm^{-2})	κ (cm^2 g^{-1})	X	Y	Z	Ω (10^{-6} rad s^{-1})
0.000001	0.00190	0.00001	1.576e+07	1.542e+02	2.368e+17	1.2914e+00	0.3364	0.6444	0.0192	1.50e-05
0.000002	0.00263	0.00002	1.576e+07	1.542e+02	2.367e+17	1.2916e+00	0.3365	0.6443	0.0192	1.50e-05
0.000003	0.00310	0.00003	1.576e+07	1.541e+02	2.367e+17	1.2917e+00	0.3366	0.6442	0.0192	1.50e-05
0.000005	0.00365	0.00005	1.576e+07	1.541e+02	2.366e+17	1.2918e+00	0.3367	0.6441	0.0192	1.50e-05
0.000009	0.00430	0.00008	1.576e+07	1.540e+02	2.366e+17	1.2920e+00	0.3369	0.6439	0.0192	1.50e-05
0.000014	0.00507	0.00013	1.575e+07	1.539e+02	2.364e+17	1.2922e+00	0.3371	0.6437	0.0192	1.50e-05
0.000023	0.00597	0.00021	1.575e+07	1.538e+02	2.363e+17	1.2926e+00	0.3375	0.6434	0.0192	1.50e-05
0.000038	0.00704	0.00034	1.574e+07	1.537e+02	2.361e+17	1.2931e+00	0.3379	0.6430	0.0191	1.50e-05
0.000062	0.00829	0.00055	1.574e+07	1.534e+02	2.357e+17	1.2938e+00	0.3385	0.6424	0.0191	1.50e-05
0.000102	0.00977	0.00089	1.573e+07	1.531e+02	2.353e+17	1.2947e+00	0.3393	0.6415	0.0191	1.50e-05
0.000166	0.01152	0.00146	1.571e+07	1.527e+02	2.347e+17	1.2960e+00	0.3405	0.6403	0.0191	1.50e-05
0.000272	0.01358	0.00238	1.570e+07	1.521e+02	2.339e+17	1.2979e+00	0.3421	0.6387	0.0191	1.50e-05
0.000444	0.01601	0.00387	1.567e+07	1.512e+02	2.328e+17	1.3004e+00	0.3444	0.6365	0.0191	1.50e-05
0.000726	0.01889	0.00629	1.564e+07	1.501e+02	2.312e+17	1.3039e+00	0.3475	0.6334	0.0191	1.49e-05
0.001187	0.02230	0.01022	1.559e+07	1.485e+02	2.291e+17	1.3087e+00	0.3517	0.6292	0.0191	1.49e-05
0.001939	0.02634	0.01655	1.552e+07	1.463e+02	2.261e+17	1.3149e+00	0.3576	0.6233	0.0191	1.48e-05
0.003168	0.03116	0.02669	1.543e+07	1.434e+02	2.221e+17	1.3236e+00	0.3656	0.6153	0.0191	1.48e-05
0.005179	0.03691	0.04284	1.530e+07	1.394e+02	2.166e+17	1.3357e+00	0.3766	0.6044	0.0191	1.47e-05
0.008465	0.04382	0.06827	1.512e+07	1.342e+02	2.092e+17	1.3526e+00	0.3914	0.5895	0.0190	1.45e-05
0.013830	0.05217	0.10770	1.488e+07	1.274e+02	1.993e+17	1.3763e+00	0.4114	0.5696	0.0190	1.43e-05
0.022608	0.06237	0.16760	1.455e+07	1.187e+02	1.863e+17	1.4098e+00	0.4378	0.5433	0.0189	1.41e-05
0.036949	0.07497	0.25560	1.410e+07	1.079e+02	1.694e+17	1.4577e+00	0.4720	0.5092	0.0188	1.37e-05
0.056968	0.08871	0.36217	1.358e+07	9.657e+01	1.509e+17	1.5169e+00	0.5091	0.4722	0.0187	1.33e-05

Table 7 *continued*

Table 7 *(continued)*

$M/M_\odot$	$r/R_\odot$	$L/L_\odot$	T (K)	ρ (g cm^{-3})	p (dyn cm^{-2})	κ (cm^2 g^{-1})	X	Y	Z	Ω (10^{-6} rad s^{-1})
0.080715	0.10213	0.46885	1.304e+07	8.624e+01	1.333e+17	1.5799e+00	0.5433	0.4380	0.0186	1.30e-05
0.109607	0.11617	0.57552	1.248e+07	7.636e+01	1.161e+17	1.6526e+00	0.5758	0.4057	0.0185	1.26e-05
0.146362	0.13193	0.68219	1.185e+07	6.642e+01	9.836e+16	1.7429e+00	0.6072	0.3744	0.0184	1.22e-05
0.196727	0.15132	0.78841	1.110e+07	5.573e+01	7.918e+16	1.8647e+00	0.6383	0.3434	0.0183	1.18e-05
0.254970	0.17201	0.87065	1.033e+07	4.595e+01	6.194e+16	2.0069e+00	0.6631	0.3188	0.0182	1.14e-05
0.312918	0.19172	0.92300	9.650e+06	3.798e+01	4.845e+16	2.1549e+00	0.6810	0.3010	0.0181	1.04e-05
0.369383	0.21066	0.95531	9.044e+06	3.149e+01	3.790e+16	2.3107e+00	0.6909	0.2911	0.0180	9.57e-06
0.423543	0.22902	0.97493	8.501e+06	2.610e+01	2.965e+16	2.4761e+00	0.6975	0.2846	0.0179	9.20e-06
0.474881	0.24694	0.98679	8.011e+06	2.160e+01	2.319e+16	2.6534e+00	0.7022	0.2800	0.0179	8.80e-06
0.523093	0.26456	0.99366	7.567e+06	1.786e+01	1.814e+16	2.8464e+00	0.7054	0.2768	0.0178	8.40e-06
0.568053	0.28198	0.99705	7.162e+06	1.474e+01	1.419e+16	3.0574e+00	0.7078	0.2745	0.0177	8.03e-06
0.609743	0.29929	0.99852	6.789e+06	1.215e+01	1.110e+16	3.2874e+00	0.7098	0.2725	0.0177	7.66e-06
0.648210	0.31657	0.99923	6.446e+06	1.001e+01	8.682e+15	3.5379e+00	0.7115	0.2709	0.0177	7.31e-06
0.683576	0.33387	0.99960	6.126e+06	8.229e+00	6.792e+15	3.8109e+00	0.7129	0.2695	0.0176	6.96e-06
0.715985	0.35125	0.99980	5.829e+06	6.762e+00	5.312e+15	4.1078e+00	0.7141	0.2683	0.0176	6.64e-06
0.745591	0.36875	0.99991	5.550e+06	5.552e+00	4.156e+15	4.4296e+00	0.7151	0.2673	0.0176	6.32e-06
0.772576	0.38642	0.99997	5.287e+06	4.556e+00	3.251e+15	4.7782e+00	0.7161	0.2664	0.0175	6.02e-06
0.797116	0.40428	1.00000	5.040e+06	3.737e+00	2.543e+15	5.1556e+00	0.7169	0.2656	0.0175	5.74e-06
0.819381	0.42237	1.00001	4.806e+06	3.064e+00	1.989e+15	5.5644e+00	0.7177	0.2648	0.0175	5.46e-06
0.839548	0.44069	1.00001	4.584e+06	2.511e+00	1.556e+15	6.0050e+00	0.7186	0.2640	0.0174	5.21e-06
0.857782	0.45929	1.00001	4.373e+06	2.058e+00	1.217e+15	6.4815e+00	0.7194	0.2632	0.0174	4.96e-06
0.874233	0.47816	1.00000	4.172e+06	1.686e+00	9.520e+14	7.0002e+00	0.7203	0.2624	0.0174	4.73e-06
0.889056	0.49732	1.00000	3.980e+06	1.382e+00	7.447e+14	7.5656e+00	0.7212	0.2614	0.0174	4.51e-06
0.902387	0.51678	0.99999	3.795e+06	1.132e+00	5.825e+14	8.1805e+00	0.7223	0.2604	0.0173	4.30e-06
0.914354	0.53654	0.99998	3.618e+06	9.283e-01	4.557e+14	8.8490e+00	0.7234	0.2593	0.0173	4.11e-06

Table 7 *continued*

Table 7 *(continued)*

$M/M_\odot$	$r/R_\odot$	$L/L_\odot$	T (K)	ρ (g cm^{-3})	p (dyn cm^{-2})	κ (cm^2 g^{-1})	X	Y	Z	Ω (10^{-6} rad s^{-1})
0.925080	0.55659	0.99998	3.446e+06	7.614e-01	3.564e+14	9.5772e+00	0.7247	0.2580	0.0173	3.92e-06
0.934675	0.57691	0.99997	3.280e+06	6.251e-01	2.788e+14	1.0375e+01	0.7262	0.2565	0.0173	3.75e-06
0.943239	0.59749	0.99997	3.118e+06	5.137e-01	2.181e+14	1.1257e+01	0.7278	0.2549	0.0173	3.58e-06
0.950869	0.61828	0.99996	2.958e+06	4.230e-01	1.706e+14	1.2250e+01	0.7296	0.2531	0.0173	3.42e-06
0.957649	0.63923	0.99996	2.799e+06	3.491e-01	1.334e+14	1.3427e+01	0.7316	0.2510	0.0174	3.28e-06
0.963657	0.66025	0.99997	2.637e+06	2.894e-01	1.044e+14	1.5065e+01	0.7338	0.2485	0.0177	3.14e-06
0.968963	0.68119	0.99997	2.467e+06	2.417e-01	8.165e+13	1.6387e+01	0.7360	0.2467	0.0173	3.02e-06
0.973526	0.70160	0.99998	2.295e+06	2.041e-01	6.424e+13	1.7759e+01	0.7382	0.2454	0.0164	2.92e-06
0.976002	0.71333	1.00022	2.185e+06	1.854e-01	5.560e+13	1.8426e+01	0.7396	0.2450	0.0155	2.87e-06
0.977337	0.72008	1.00037	2.114e+06	1.764e-01	5.118e+13	1.9703e+01	0.7396	0.2450	0.0155	2.87e-06
0.980936	0.73943	1.00030	1.918e+06	1.522e-01	4.004e+13	2.3806e+01	0.7396	0.2450	0.0155	2.87e-06
0.984045	0.75784	1.00024	1.741e+06	1.313e-01	3.132e+13	2.8373e+01	0.7396	0.2450	0.0155	2.87e-06
0.986711	0.77528	1.00019	1.579e+06	1.133e-01	2.450e+13	3.3468e+01	0.7396	0.2450	0.0155	2.87e-06
0.988982	0.79177	1.00016	1.433e+06	9.775e-02	1.916e+13	3.9246e+01	0.7396	0.2450	0.0155	2.87e-06
0.990904	0.80729	1.00013	1.300e+06	8.435e-02	1.499e+13	4.5830e+01	0.7396	0.2450	0.0155	2.87e-06
0.992521	0.82188	1.00011	1.180e+06	7.278e-02	1.173e+13	5.3219e+01	0.7396	0.2450	0.0155	2.87e-06
0.993874	0.83555	1.00009	1.070e+06	6.280e-02	9.173e+12	6.1516e+01	0.7396	0.2450	0.0155	2.87e-06
0.995001	0.84832	1.00008	9.710e+05	5.419e-02	7.175e+12	7.0972e+01	0.7396	0.2450	0.0155	2.87e-06
0.995933	0.86022	1.00007	8.811e+05	4.677e-02	5.613e+12	8.2430e+01	0.7396	0.2450	0.0155	2.87e-06
0.996702	0.87130	1.00006	7.995e+05	4.036e-02	4.390e+12	9.6834e+01	0.7396	0.2450	0.0155	2.87e-06
0.997334	0.88158	1.00006	7.254e+05	3.483e-02	3.434e+12	1.1441e+02	0.7396	0.2450	0.0155	2.87e-06
0.997850	0.89110	1.00005	6.583e+05	3.006e-02	2.686e+12	1.3527e+02	0.7396	0.2450	0.0155	2.87e-06
0.998271	0.89991	1.00005	5.975e+05	2.594e-02	2.101e+12	1.5967e+02	0.7396	0.2450	0.0155	2.87e-06
0.998613	0.90804	1.00005	5.423e+05	2.239e-02	1.644e+12	1.8885e+02	0.7396	0.2450	0.0155	2.87e-06
0.998889	0.91554	1.00005	4.923e+05	1.932e-02	1.286e+12	2.2482e+02	0.7396	0.2450	0.0155	2.87e-06

Table 7 *continued*

Table 7 *(continued)*

$M/M_\odot$	$r/R_\odot$	$L/L_\odot$	T (K)	ρ (g cm^{-3})	p (dyn cm^{-2})	κ (cm^2 g^{-1})	X	Y	Z	Ω (10^{-6} rad s^{-1})
0.999113	0.92244	1.00005	4.469e+05	1.668e-02	1.006e+12	2.7065e+02	0.7396	0.2450	0.0155	2.87e-06
0.999292	0.92878	1.00005	4.058e+05	1.439e-02	7.867e+11	3.3250e+02	0.7396	0.2450	0.0155	2.87e-06
0.999436	0.93461	1.00005	3.685e+05	1.242e-02	6.154e+11	4.1670e+02	0.7396	0.2450	0.0155	2.87e-06
0.999552	0.93995	1.00004	3.348e+05	1.072e-02	4.814e+11	5.3263e+02	0.7396	0.2450	0.0155	2.87e-06
0.999644	0.94484	1.00004	3.042e+05	9.247e-03	3.765e+11	6.9405e+02	0.7396	0.2450	0.0155	2.87e-06
0.999718	0.94933	1.00004	2.765e+05	7.979e-03	2.946e+11	9.2024e+02	0.7396	0.2450	0.0155	2.87e-06
0.999777	0.95343	1.00004	2.514e+05	6.883e-03	2.304e+11	1.2436e+03	0.7396	0.2450	0.0155	2.87e-06
0.999823	0.95718	1.00004	2.288e+05	5.936e-03	1.802e+11	1.7082e+03	0.7396	0.2450	0.0155	2.87e-06
0.999860	0.96060	1.00004	2.083e+05	5.118e-03	1.410e+11	2.3811e+03	0.7396	0.2450	0.0155	2.87e-06
0.999890	0.96373	1.00004	1.898e+05	4.411e-03	1.103e+11	3.3552e+03	0.7396	0.2450	0.0155	2.87e-06
0.999913	0.96659	1.00004	1.731e+05	3.798e-03	8.626e+10	4.7501e+03	0.7396	0.2450	0.0155	2.87e-06
0.999931	0.96921	1.00004	1.581e+05	3.269e-03	6.748e+10	6.6841e+03	0.7396	0.2450	0.0155	2.87e-06
0.999946	0.97159	1.00004	1.447e+05	2.810e-03	5.278e+10	9.2032e+03	0.7396	0.2450	0.0155	2.87e-06
0.999957	0.97378	1.00004	1.326e+05	2.412e-03	4.129e+10	1.2213e+04	0.7396	0.2450	0.0155	2.87e-06
0.999967	0.97578	1.00004	1.217e+05	2.068e-03	3.230e+10	1.5468e+04	0.7396	0.2450	0.0155	2.87e-06
0.999974	0.97761	1.00004	1.118e+05	1.772e-03	2.526e+10	1.8710e+04	0.7396	0.2450	0.0155	2.87e-06
0.999979	0.97930	1.00004	1.028e+05	1.516e-03	1.976e+10	2.1823e+04	0.7396	0.2450	0.0155	2.87e-06
0.999984	0.98084	1.00004	9.461e+04	1.298e-03	1.546e+10	2.4907e+04	0.7396	0.2450	0.0155	2.87e-06
0.999987	0.98225	1.00004	8.699e+04	1.111e-03	1.209e+10	2.8321e+04	0.7396	0.2450	0.0155	2.87e-06
0.999990	0.98355	1.00004	7.994e+04	9.521e-04	9.458e+09	3.2562e+04	0.7396	0.2450	0.0155	2.87e-06
0.999994	0.98581	1.00004	6.744e+04	7.004e-04	5.788e+09	4.5889e+04	0.7396	0.2450	0.0155	2.87e-06
0.999996	0.98771	1.00004	5.714e+04	5.143e-04	3.541e+09	6.9908e+04	0.7396	0.2450	0.0155	2.87e-06
0.999998	0.98929	1.00004	4.894e+04	3.749e-04	2.167e+09	1.0278e+05	0.7396	0.2450	0.0155	2.87e-06
0.999999	0.99064	1.00004	4.252e+04	2.701e-04	1.326e+09	1.2664e+05	0.7396	0.2450	0.0155	2.87e-06
0.999999	0.99179	1.00004	3.746e+04	1.923e-04	8.113e+08	1.2530e+05	0.7396	0.2450	0.0155	2.87e-06

Table 7 *continued*

Table 7 *(continued)*

$M/M_\odot$	$r/R_\odot$	$L/L_\odot$	T (K)	ρ (g cm^{-3})	p (dyn cm^{-2})	κ (cm^2 g^{-1})	X	Y	Z	Ω (10^{-6} rad s^{-1})
0.999999	0.99231	1.00004	3.531e+04	1.616e-04	6.346e+08	1.1637e+05	0.7396	0.2450	0.0155	2.87e-06
0.999999	0.99279	1.00004	3.337e+04	1.355e-04	4.964e+08	1.0456e+05	0.7396	0.2450	0.0155	2.87e-06
1.000000	0.99354	1.00004	3.044e+04	9.966e-05	3.255e+08	8.2105e+04	0.7396	0.2450	0.0155	2.87e-06
1.000000	0.99444	1.00004	2.716e+04	6.534e-05	1.845e+08	5.6764e+04	0.7396	0.2450	0.0155	2.87e-06
1.000000	0.99594	1.00004	2.214e+04	2.646e-05	5.699e+07	2.3956e+04	0.7396	0.2450	0.0155	2.87e-06
1.000000	0.99786	1.00004	1.643e+04	4.852e-06	6.879e+06	4.6756e+03	0.7396	0.2450	0.0155	2.87e-06
1.000000	0.99837	1.00004	1.495e+04	2.667e-06	3.292e+06	2.5776e+03	0.7396	0.2450	0.0155	2.87e-06
1.000000	0.99881	1.00004	1.360e+04	1.469e-06	1.576e+06	1.3462e+03	0.7396	0.2450	0.0155	2.87e-06
1.000000	0.99919	1.00004	1.230e+04	8.173e-07	7.542e+05	6.2276e+02	0.7396	0.2450	0.0155	2.87e-06
1.000000	0.99952	1.00004	1.090e+04	4.663e-07	3.610e+05	2.0916e+02	0.7396	0.2450	0.0155	2.87e-06
1.000000	0.99979	1.00004	8.935e+03	2.874e-07	1.728e+05	2.7659e+01	0.7396	0.2450	0.0155	2.87e-06
1.000000	0.99998	1.00004	6.028e+03	2.073e-07	8.270e+04	5.0052e-01	0.7396	0.2450	0.0155	2.87e-06
1.000000	1.00002	1.00004	5.777e+03	1.719e-07	6.569e+04	3.1819e-01	0.7396	0.2450	0.0155	2.87e-06